Supplementary Information (SI) for Energy & Environmental Science.

Breaking the H_2O dissociation-OH desorption scaling relationship in alkaline hydrogen evolution by oxophilic single atom M_1-Ru_n electrocatalyst

Xinhu Liang,[#a] Zhihao Zhang,[#b] Zhe Wang,[#a] Mingzhen Hu,[*ab] Dan Cheng,[c] Yue Jiang,[a] Hao Ren,[a] Fengyi Shen,[a] Shitu Yang,[a] Xiaoxin Yang,[a] Wenkun Jiang,[a] Xianghui Shi,[a] Zihao Ma,[a] and Kebin Zhou[*abd]

---

[a] *School of Chemical Sciences, University of Chinese Academy of Sciences, Beijing, 100049, PR China. E-mail: humingzhen12@ucas.ac.cn; kbzhou@ucas.ac.cn*

[b] *National Engineering Laboratory for VOCs Pollution Control Material & Technology, Research Center for Environmental Material and Pollution Control Technology, University of Chinese Academy of Sciences, Beijing, 100049, PR China.*

[c] *College of Pharmacy, Shandong Second Medical University, Weifang, 261053, PR China.*

[d] *Binzhou Institute of Technology, Weiqiao-UCAS Science and Technology Park, Binzhou, 256606, Shandong Province, China.*

[#] *These authors contributed equally to this work.*

Electronic Supplementary Information (ESI) available: [details of any supplementary information available should be included here]. See DOI: 10.1039/x0xx00000x

Experimental Section

Materials: All chemicals were of analytical grade and used as received without further purification. Tris(hydroxymethyl)aminomethane was purchased from the Alfa Aesar Chemicals Co., Ltd. Zinc nitrate hexahydrate, iron chloride hexahydrate and concentrated hydrochloric acid were acquired from the Sinopharm Chemical Reagent Co., Ltd. Ruthenium chloride was obtained from the Macklin Biochemical Co., Ltd. Molybdenum powder. samarium nitrate hexahydrate, lanthanum nitrate hexahydrate, dopamine hydrochloride and sodium hydroxide were purchased from the Aladdin Biochemical Technology Co., Ltd. Hydrogen peroxide and concentrated nitric acid were bought from the Beijing Institute of Chemical Reagents Co.,Ltd. The 20% Pt/C catalysts was purchased from the Sigma-Aldrich. Ethanol were obtained from the Tongguang Fine Chemical Company Beijing.

Preparation of $La(OH)_3$ nanorods: $La(OH)_3$ nanorods were synthesized according to previous report.[1] In a typical preparation, 11.54 g of $La(NO_3)_3 \cdot 6H_2O$ was sufficiently dissolved in 20 mL of deionized water and 40 mL of 18 M NaOH solution was then added to make a homogeneous system. After stirring thoroughly for 30 min, the suspension was transferred to a 100 mL Teflon-lined autoclave and heated at 110 °C for 24 hours. When the autoclave was cooled down to room temperature, centrifugation and washing procedures were further conducted to clean the solid products. Finally, the acquired solid products were dried in oven at 100 °C overnight.

Preparation of $Sm(OH)_3$ nanorods: $Sm(OH)_3$ nanorods were prepared taking similar procedures to that of the $La(OH)_3$ nanorods except for using using 11.81 g of $Sm(NO_3)_3 \cdot 6H_2O$ instead of $La(NO_3)_3 \cdot 6H_2O$.

Preparation of MoO_2 nanorods: MoO_2 nanorods were synthesized modified from previous report[2]: 7.5 ml of H_2O_2 was slowly added to 0.75 g of molybdenum powder drop by drop (caution this is a very exothermal process) under mild stirring. After which, 37.5 ml of deionized water and 15 ml of ethanol was added the above obtained solution in sequence and further stirred for 30 min. The acquired orange solution was then transferred to a 100 ml Teflon-lined autoclave and heated at 200 °C for 72 hours. After the autoclave was cooled to room temperature, the product was collected by centrifugation and washed several times with ethanol, and then dried in vacuum oven at 60 °C for 24 hours.

Preparation of α-FeOOH nanorods: α-FeOOH nanorods were synthesized as follows[3]: 3.2 g of $FeCl_3 \cdot 6H_2O$ was firstly dissolved in 30 ml of deionized water, and 30 ml of 2 M NaOH solution was then added to the above solution under mild stirring. The obtained products were washed several times by deionized water and then dissolved in 60 ml 2 M NaOH solution to allow for stirring vigorously for 30 min. The suspension was further transferred to a 100 ml Teflon-lined autoclave and heated to 160°C for 20 hours. After the autoclave was cooled down to room temperature, the product was collected by centrifugation and washed several times with deionized water, and dried in oven at 80 °C overnight.

Preparation of ZnO nanorods: ZnO nanorods was prepared by the following procedures.[4] 7.434 g of $Zn(NO_3)_2·6H_2O$ was dissolved in 45 ml of deionized water, 32 ml of 1.5 M KOH solution was then added drop by drop to the above solution, stirred vigorously for 30 min. Subsequently, the obtained suspension was transferred to a 100 ml Teflon-lined autoclave and heated at 110 °C for 20 hours. After the autoclave was cooled down to room temperature, the product was collected by centrifugation and washed several times with deionized water and then dried in oven at 120 °C for 12 hours.

PDA coating treatment and thermal transition of the M-containing oxides/hydroxides nanorods: Taking the PDA coating of $La(OH)_3$ nanorods as an example. To begin with, 0.5 g of $La(OH)_3$ nanorods and 0.2432 g of Tris were added to 200 ml of deionized water and sonicated for 1 hour to obtain a suspension. After which, 0.5 g of dopamine hydrochloride dissolved in 20 ml of deionized water was added to the above suspension under mild stirring. The mixed solution was further stirred at room temperature for 12 hours to assure efficient PDA coating. The acquired solid products were collected by centrifugation and washed with deionized water and ethanol for several times , and then dried in an oven at 60 °C overnight to obtain the $La(OH)_3$@PDA intermediates. Subsequently, $La(OH)_3$@PDA was firstly pyrolyzed at 500 °C for 2 hours, and then at 800 °C for 2 hours under argon. After thermal annealing, the obtained La_2O_3@NC was selectively etched by hydrochloric acid or the mixture of hydrochloric acid, hydrogen peroxide, and nitric acid at 65 ^oC to attain the La_2O_3/NC or the La_1/NC products, respectively. The preparation of other M_xO_y/NC or M_1/NC products were similar to the La_2O_3/NC or the La_1/NC.

Preparation of the M_xO_y-Ru_n/NC catalysts: The preparation of the M_{xOy}-Ru_n/NC catalysts were based on impregnation route. Taking the synthesis of the La_2O_3-Ru_n/NC catalyst as an example. Firstly, 199 ul of 0.1 M $RuCl_3$ solution was added to 10 ml of deionized water. After which, 0.02 g of La_2O_3/NC support was added to the above solution and mildly stirring for 12 hours. The solid products were obtained by centrifugation and dried in an oven at 60 °C overnight. Finally, the acquired solid powders were reduced with hydrogen at 300 °C for 2 hours. Other M_xO_y-Ru_n/NC catalysts were prepared similarly to that of the La_2O_3-Ru_n/NC catalyst.

Preparation of the M_1-Ru_n/NC catalysts: M_1-Ru_n/NC samples were synthesized in the same way to the M_xO_y-Ru_n/NC catalyst, except for taking the M_1/NC as the support rather than the M_xO_y/NC.

Materials characterization: The crystallographic structures of materials were collected by the powder X-ray diffraction (XRD, Bruker D8 ADVANCE, Cu Kα radiation, λ =1.5406 Å). The element amounts of catalyst were determined by the inductively coupled plasma optical emission spectrometer (ICP-OES) of Aligent ICPOES730. Transmission election microscope (TEM) images and scanning transmission election microscope (STEM) images were collected on the FEI Talos F200X (Thermo) operated at 200 kV. Atomic resolved STEM observation was carried out on Themis Z (Titancubed·ThemisZ: 300kV·Thermo-Fisherscientific). The X-ray photoelectron spectroscopy (XPS) spectra were obtained by the Thermo Fisher QXi X-ray Photoelectron Spectrometer. The XAFS experiments were performed on beamline BL14W1 at the Shanghai Synchrotron Radiation Facility (SSRF). All the spectra data were collected at ambient temperature. The X-ray absorption near edge structure (XANES) and extended X-ray absorption fine structure (EXAFS) profiles were analyzed by the Athena and Artemis modules implemented in the IFEFFIT software packages. The k^3 -weighted EXAFS spectra were obtained via subtracting the background from the overall absorption and normalized based on the edge-jump step. In order to attain the quantitative coordination information of the interested atoms, the least-squares curve parametes were fitted to the EXAFS spectra by virtue of the ARTEMIS module.

Electrochemical measurements: A standard three-electrode testing system with a CHI 760E electrochemical workstation was employed to evaluate the alkaline HER performances of catalysts that was performed in 1 M KOH solution without iR compensation. Graphite rod, Hg/HgO electrode and glassy carbon electrode (GCE), were used as the counter electrode, reference electrode and working electrode, respectively. All the reaction potentials mentioned in this work were normalized to the reversible hydrogen electrode (RHE) through the following equation: $E_{\mathrm{RHE}} = E_{\mathrm{Hg/HgO}} + 0.0591 \times \mathrm{pH} + 0.098$. The working electrode was functionalized as follows, 1 mg of catalyst was homogeneously dispersed in 150 μL solution containing 65 μL of water, 65 μL of isopropanol and 20 μL of Nafion under sonication. Subsequently, 0.8 μL of the as-made ink was dropped onto the a polished GCE and naturally dried in air. The polarization curves were obtained by sweeping the potential from 0.1 to −0.39 V at a scan rate of 10 mV s^{-1} with iR-compensation. The stability test of the catalysts was performed by the chronopotentiometric technique at a current density of 60 mA/cm^{-2} via coating 7.5 μL of the above-mentioned ink on 0.5 cm^2 hydrophilic carbon paper performed at a H-cell. Accelerated durability tests (ADT) were performed on GCE by cycling between 0.06 and −0.15 V for 4000 cycles at room temperature. The EIS measurements were carried out at a reaction potential of 50 mV with a 5 mV amplitude and a frequency range from 1000,000 to 0.01 Hz.

In situ Raman measurements: The in situ Raman spectra were recorded on an inVia Reflex instrument with a confocal microscope. During the test, all the spectra were acquired at room temperature with a 532 nm excitation. Calibration was conducted using the 520 cm^{-1} peak (silicon wafer standard). To avoid damage samples, the power of laser was decreased by a factor of 10. In situ Raman measurements were carried out on a home-made electrochemical reaction cell using a standard three-electrode system containing 1.0 M KOH electrolyte. The Ag/AgCl electrode and platinum wire were used as the reference electrode and counter electrode, respectively. To make the working electrode, catalyst was firstly ultrasonically dispersed in 150 μL solvent (65 μL H_2O, 65 μL isopropanol and 20 μL Nafion). Subsequently, 5 μL of the homogeneous ink was dropped onto a carbon paper with an area of 1 cm^2. The in situ Raman data were obtained by the chronoamperometry measurements in the potential range from 0 mV to -70 mV. The spectra were recorded at steady-state conditions by holding at the desired potential for at least 120 s.

CO stripping measurements: The CO stripping measurements were carried out in 1.0 M KOH solution using a standard three-electrode system. Before the test, Argon gas was bubbled in the KOH solution for at least 30 min to remove the dissolved oxygen. CO gas (40 vol%) was then bubbled into the solution for 30 min with chronoamperometry test at 0 V vs. RHE to ensure sufficient adsorption of CO on the surface of catalyst. The electrode was then quickly transferred into an argon-saturated fresh 1.0 M KOH solution. The CO stripping current was acquired by the cyclic vlotammetry in the potential range from 0 to 1.2 V vs. RHE with a scan rate of 50 mV s^{-1}.

Device-level alkaline water electrolysis evaluation: The device was composed of the cathode (La_1-Ru_n/NC or commercial 20wt.% Pt/C coated on carbon paper), anode (Nickel foam), and the commercial AEM membrane (Fumasep FAA-3-PK-130). In detail, Nickel foam and the membrane were firstly immersed in 1 M KOH solution and 0.5 M NaCl solution for at least 24 hours prior to test. The anode was functionalized by an air-spraying route. During the test, the Ru and Pt loadings were controlled to be 0.03 mg cm^{-2} and 0.2 mg cm^{-2},respectively. Subsequently, the cathode, membrane and anode were integrated between two Ti bipolar plates to obtain the assembly device. The water electrolysis was operated at 80 ^{o}C under ambient pressure using 1.0 M KOH as the electrolyte on anodic side. Polarization curves were obtained from 0.05 to 6.0 A·cm^{-2} at a stepwise rate of 0.05 A·cm^{-2}. The stability test was performed by the chronopotentiometry technique at varied current densities.

DFT calculations: The slab structural models of single atom catalysts and metal oxide cluster catalysts were constructed by taking consideration of the EXAFS fitting data in Table S1. A 15 Å-thick vacuum was introduced in the z-direction to avoid artificial interaction between periodic images. Periodic spin-polarized DFT calculations were conducted by virtue of the Vienna Ab-initio simulation package (VASP 5.4.4) with the r^2SCAN meta-generalized gradient approximation (meta-GGA) functional and DFT-D4 corrections.[5] The core electrons were demonstrated through the projected augmented wave (PAW) method.[6] Wherein, the valence electrons (La: *5s5p6s5d*, Sm: *5s4d5p6s4f*, Ru: *4p5s4d*, Mo: *4s4p5s4d*, Zn: *4s3d*, Fe: *3p4s3d*, O: *2s2p*, N: *2s2p*, C: *2s2p*, H: *1s*) were expanded on plane-wave basis sets with a cutoff energy of 520 eV. A gamma point sampling based on the Monkhorst-Pack method was employed to calculate the slab structures. The self-consistent calculations applied a convergence energy threshold of 10^{-6} eV and a force threshold of 0.02 eV $Å^{-1}$. The climbing image nudge elastic band (CI-NEB) method[7] was conducted to demonstrate the energy barriers of the transition states during the H_2O dissociation. The Gibbs free energy changes were acquired by the equation $\Delta G = \Delta E + \Delta ZPE - T\Delta S$, where ΔZPE and ΔS were the changes in zero-point energy and entropy, as determined by considering the adsorbed species and water molecules in the harmonic vibrational mode. The off-resonance Raman activities were calculated through the phonons and macroscopic dielectric tensor obtained from VASP (https://github.com/raman-sc/VASP).

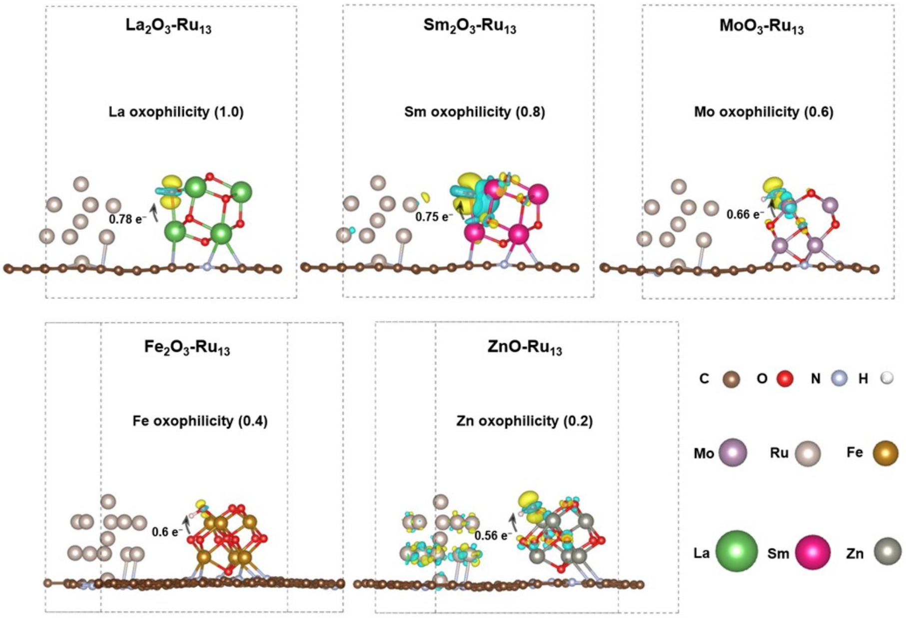

Fig. S1. Charge density difference analysis of OH adsorption over the M_xO_y-Ru_{13} catalysts (M = La, Sm, Mo, Fe, Zn).

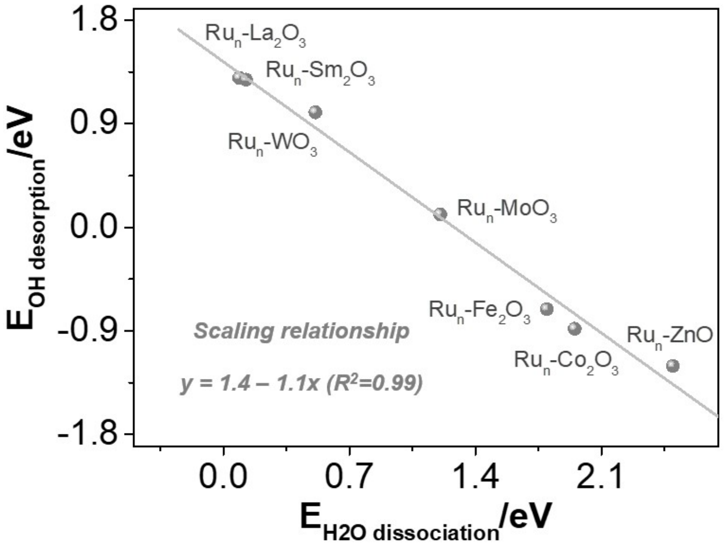

Fig. S2. The plots of OH desorption energies of the M_xO_y-Ru_{13} catalyst (M=La, Sm, Mo, Fe, Zn, W, Co) against their water dissociation energies.

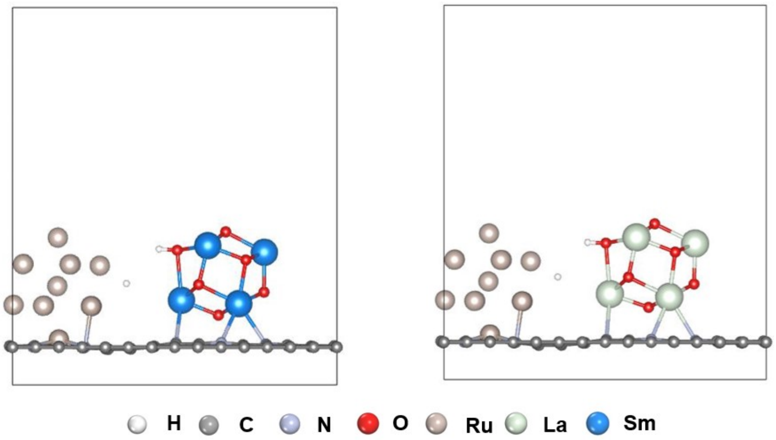

Fig. S3. The OH adsorption patterns on the Sm_2O_3-Ru_{13} model and the La_2O_3-Ru_{13} model, respectively.

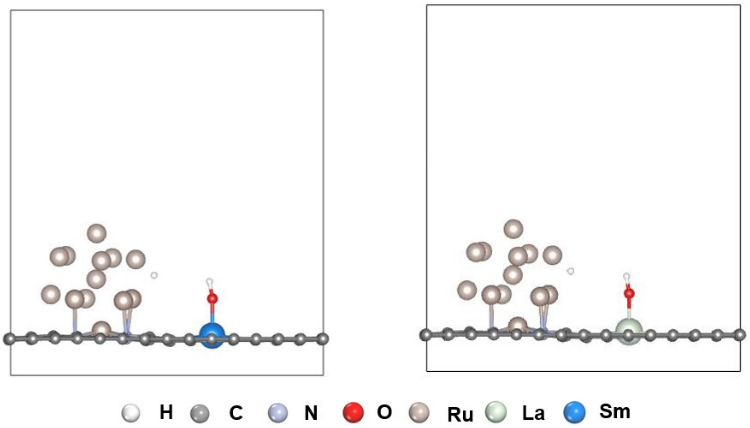

Fig. S4. The OH adsorption patterns on the Sm_1-Ru_{13} model and the La_1-Ru_{13} model, respectively.

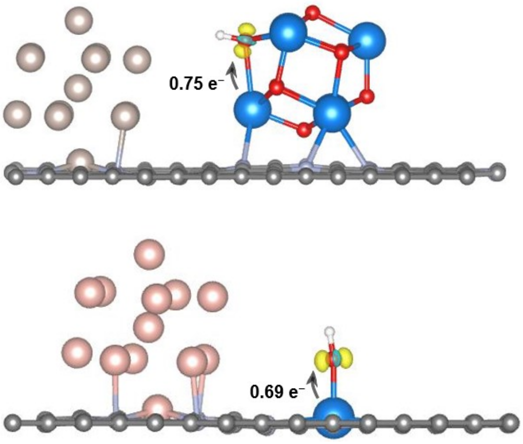

Fig. S5. Charge density difference of OH adsorption on the Sm_2O_3-Ru_{13} catalyst and Sm_1-Ru_{13} catalyst, respectively.

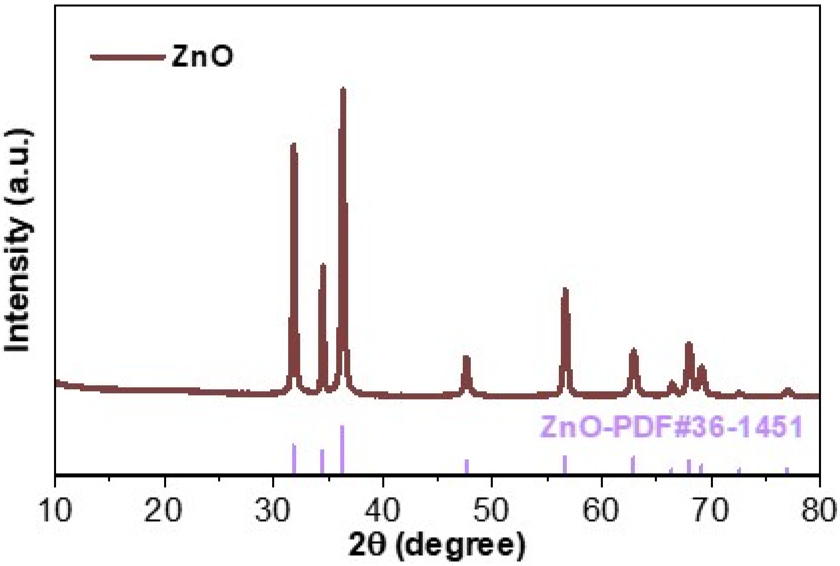

Fig. S6. The XRD patterns of the ZnO nanorods. The vertical lines represent for the standard peaks of ZnO (PDF no. 36-1451).

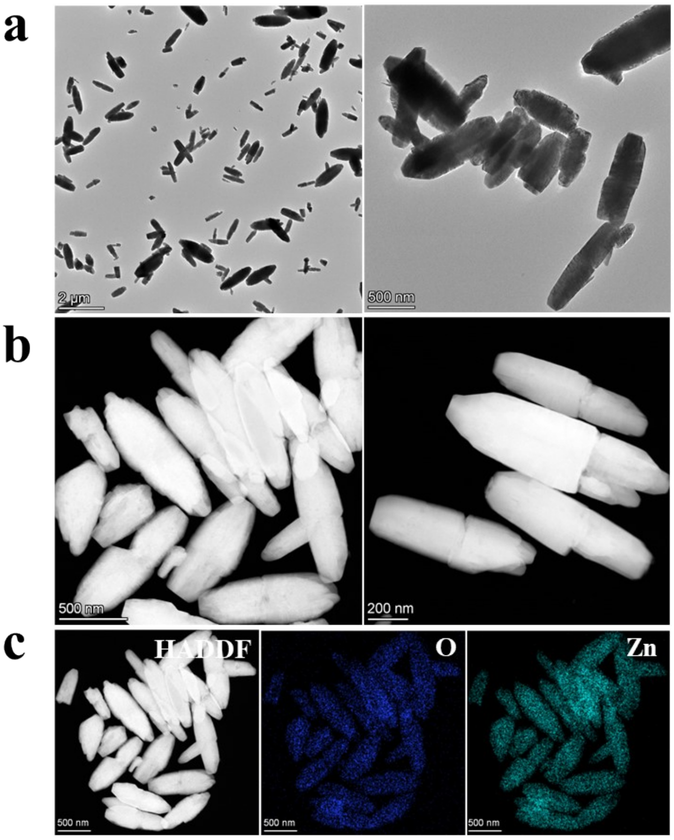

Fig. S7. (a) TEM images, (b) STEM images and (c) EDS mapping images of the prepared ZnO nanorods.

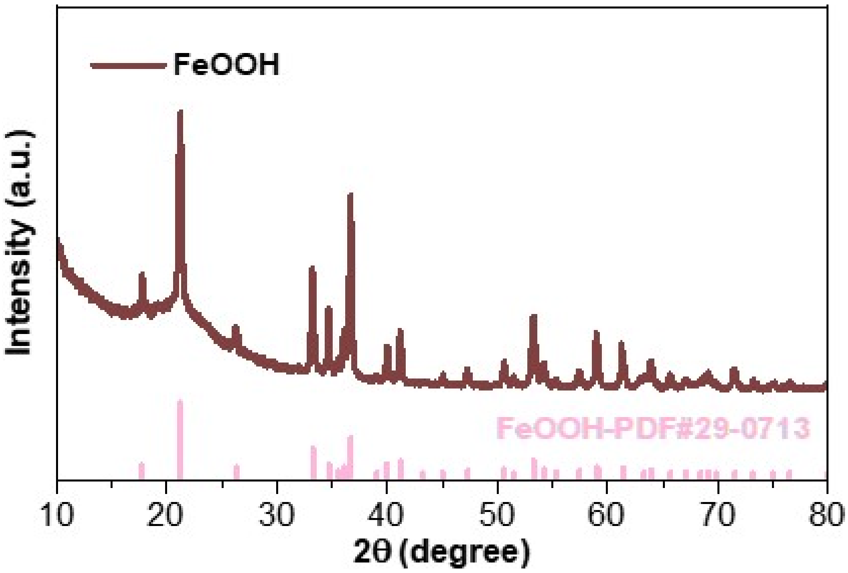

Fig. S8. The XRD patterns of the obtained FeOOH nanorods. The vertical lines represent for the standard peaks of FeOOH (PDF no. 29-0713).

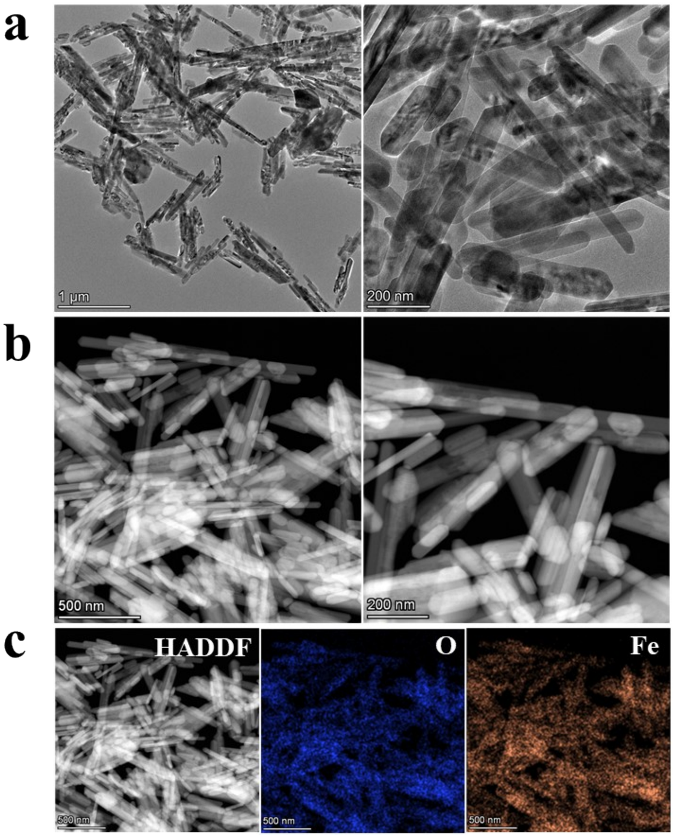

Fig. S9. (a) TEM images, (b) STEM images and (c) EDS mapping images of the as-synthesized FeOOH nanorods.

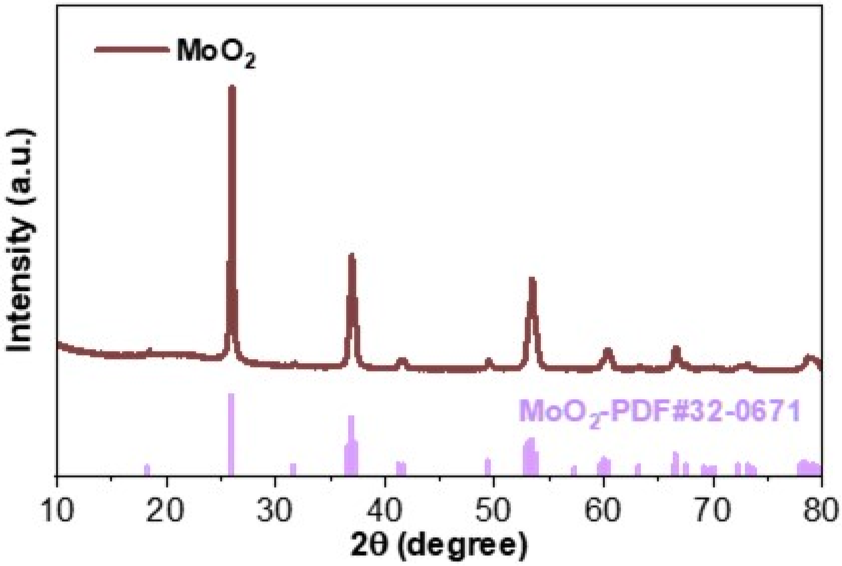

Fig. S10. The XRD patterns of the acquired MoO_2 nanorods. The vertical lines represent for the standard peaks of MoO_2 (PDF no. 32-0671).

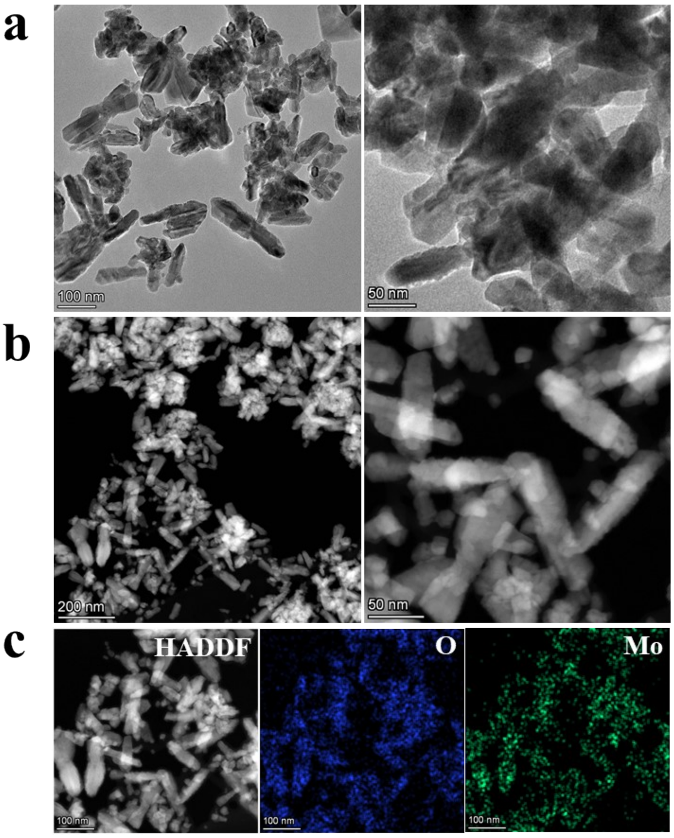

Fig. S11. (a) TEM images, (b) STEM images and (c) EDS mapping images of the synthesized MoO_2 nanorods.

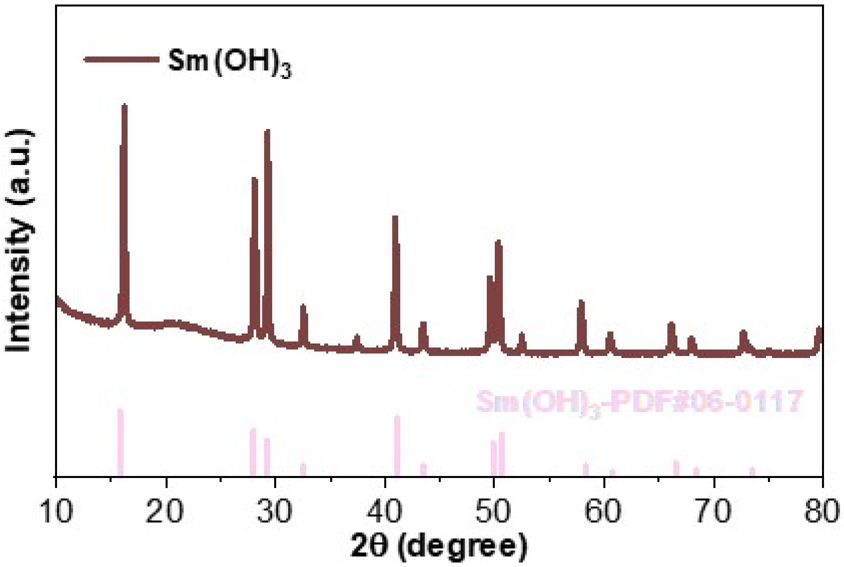

Fig. S12. The XRD patterns of the acquired $Sm(OH)_3$ nanorods. The vertical lines represent for the standard peaks of $Sm(OH)_3$ (PDF no. 06-0117).

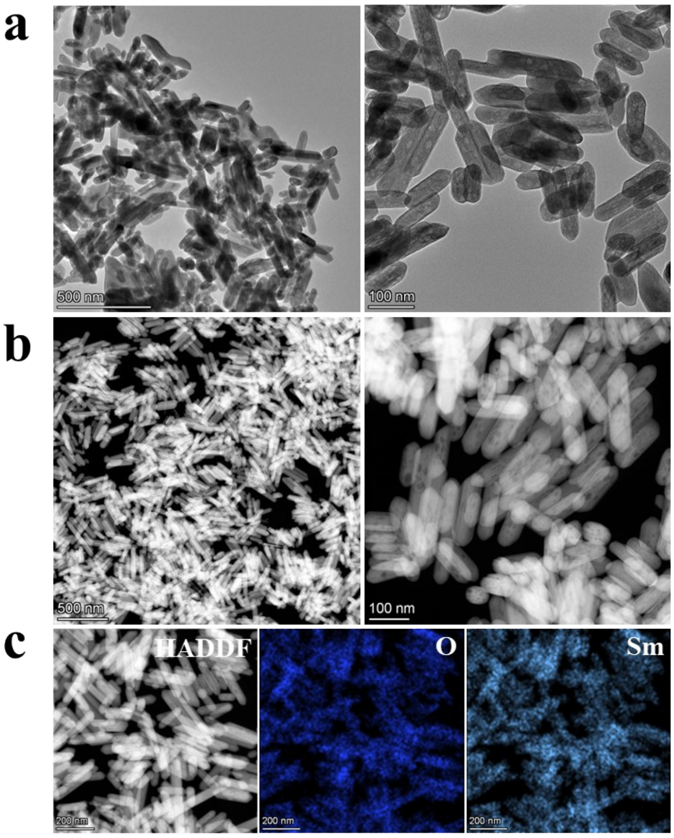

Fig. S13. (a) TEM images, (b) STEM images and (c) EDS mapping images of the prepared $Sm(OH)_3$ nanorods.

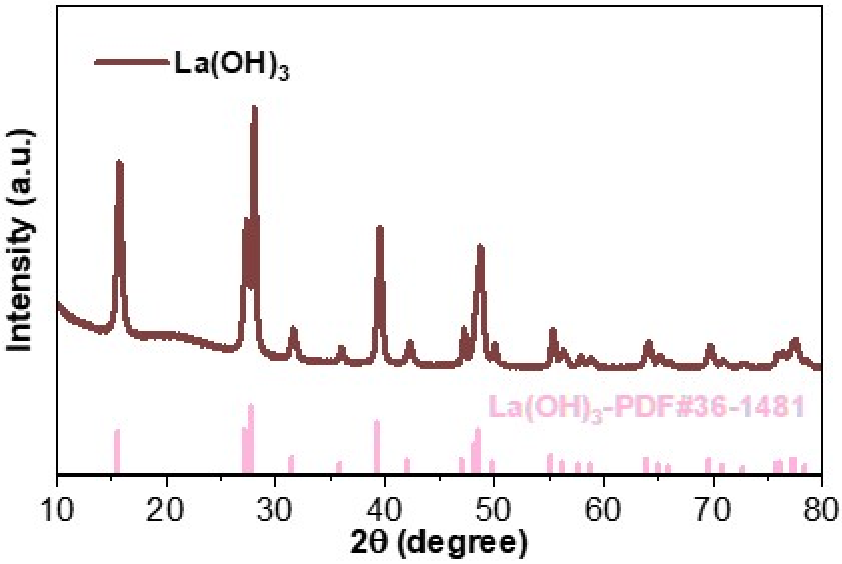

Fig. S14. The XRD patterns of the acquired La(OH)$_3$ nanorods. The vertical lines represent for the standard peaks of La(OH)$_3$ (PDF no. 36-1481).

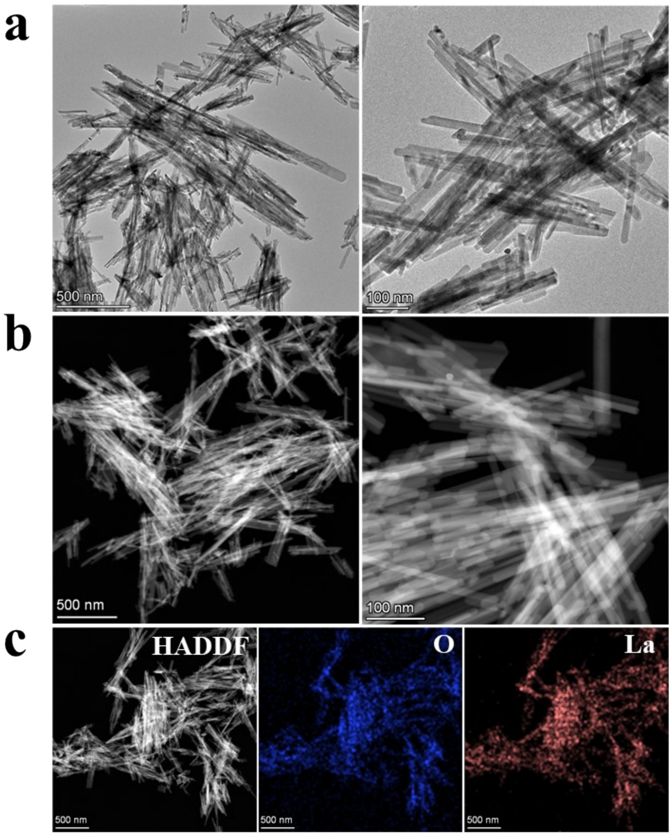

Fig. S15. (a) TEM images, (b) STEM images and (c) EDS mapping images of the synthesized La(OH)$_3$ nanorods.

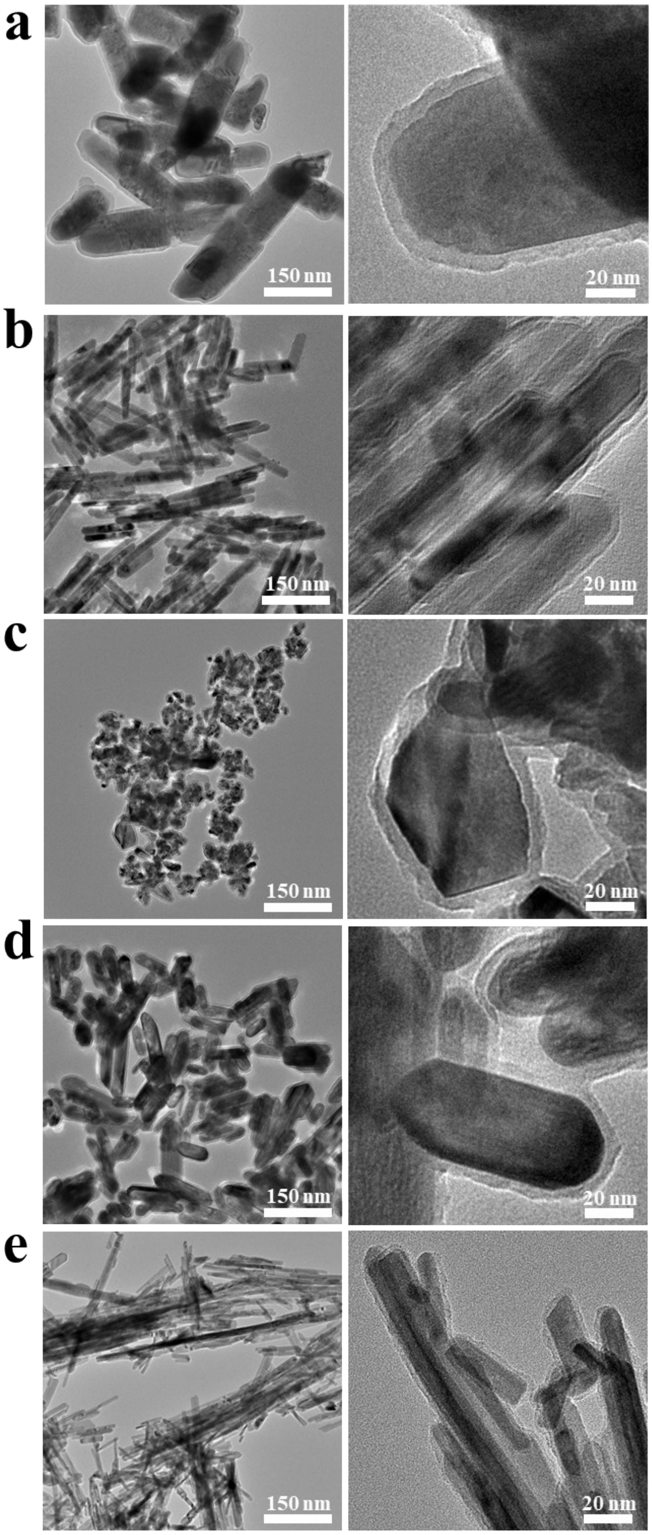

Fig. S16. TEM images of (a) ZnO@PDA, (b) FeOOH@PDA, (c) MoO_2@PDA, (d) $Sm(OH)_3$@PDA and (e) $La(OH)_3$@PDA.

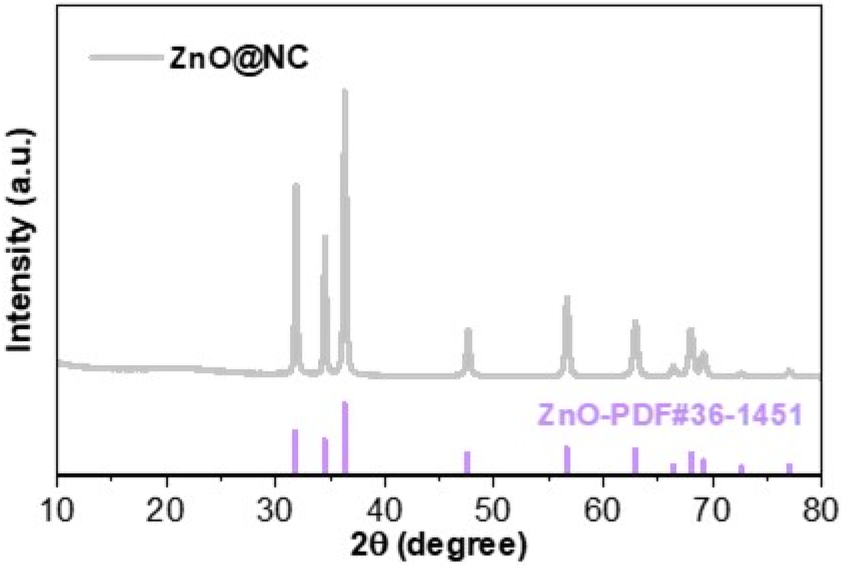

Fig. S17. The XRD patterns of the acquired ZnO@NC nanorods. The vertical lines represent for the standard peaks of ZnO (PDF no. 36-1451).

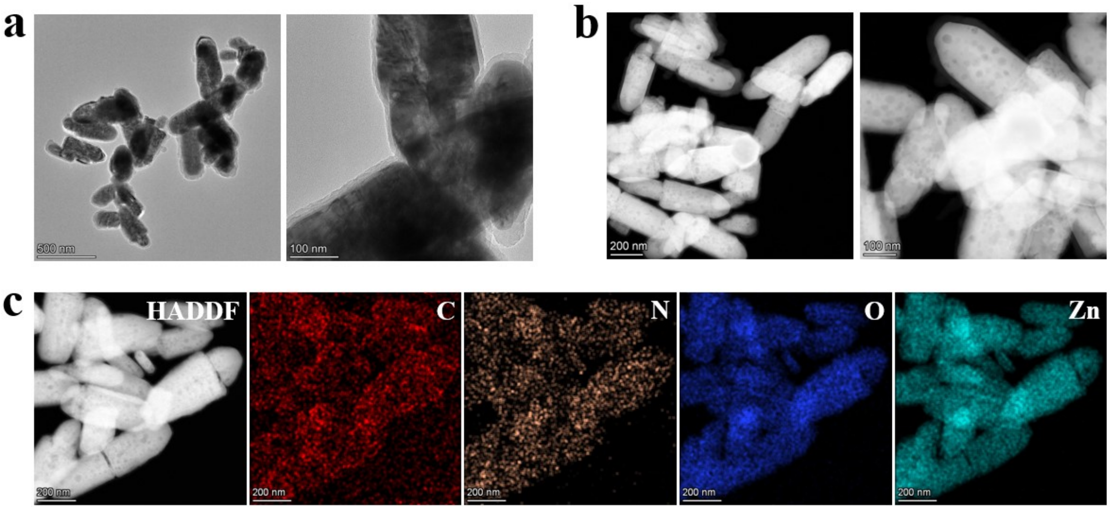

Fig. S18. (a) TEM images , (b) STEM images and (c) EDS mapping images of the ZnO@NC.

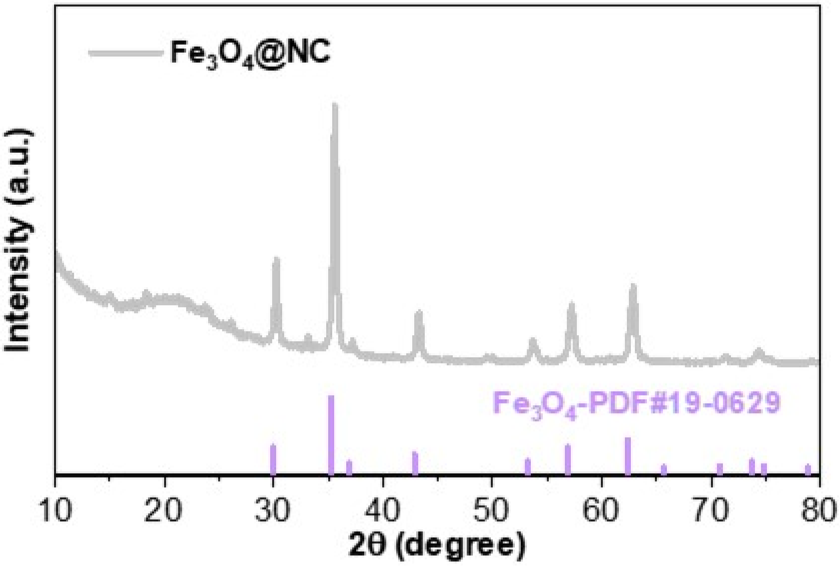

Fig. S19. The XRD patterns of the prepared Fe$_3$O$_4$@NC nanorods. The vertical lines represent for the standard peaks of Fe$_3$O$_4$ (PDF no. 19-0629).

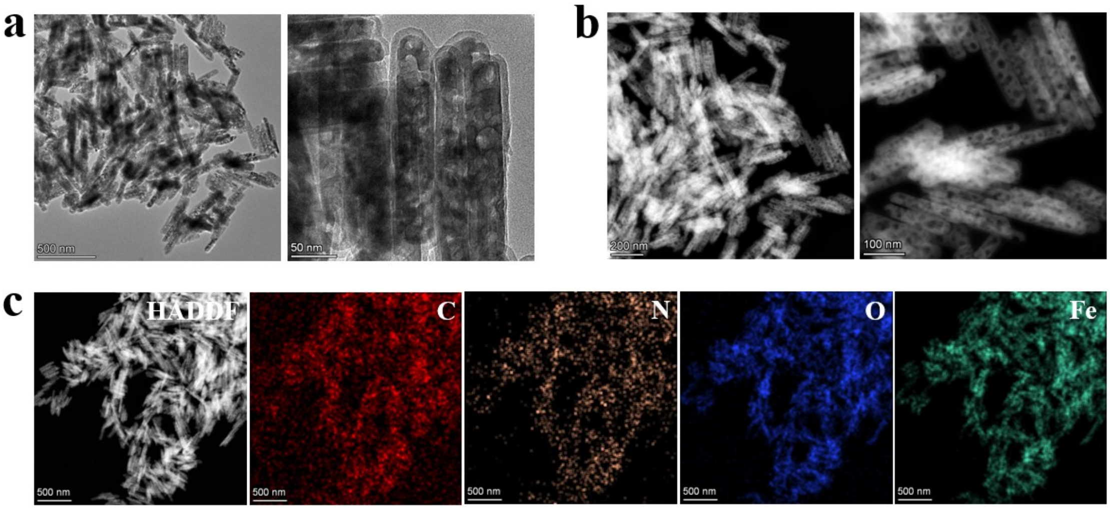

Fig. S20. (a) TEM images , (b) STEM images and (c) EDS mapping images of the Fe$_3$O$_4$@NC.

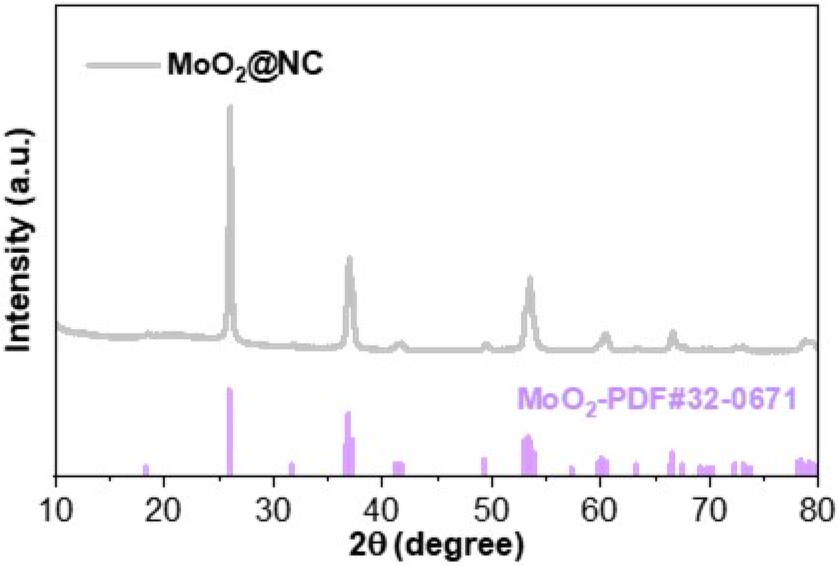

Fig. S21. The XRD patterns of the prepared MoO$_2$@NC nanorods. The vertical lines represent for the standard peaks of MoO$_2$ (PDF no. 32-0671).

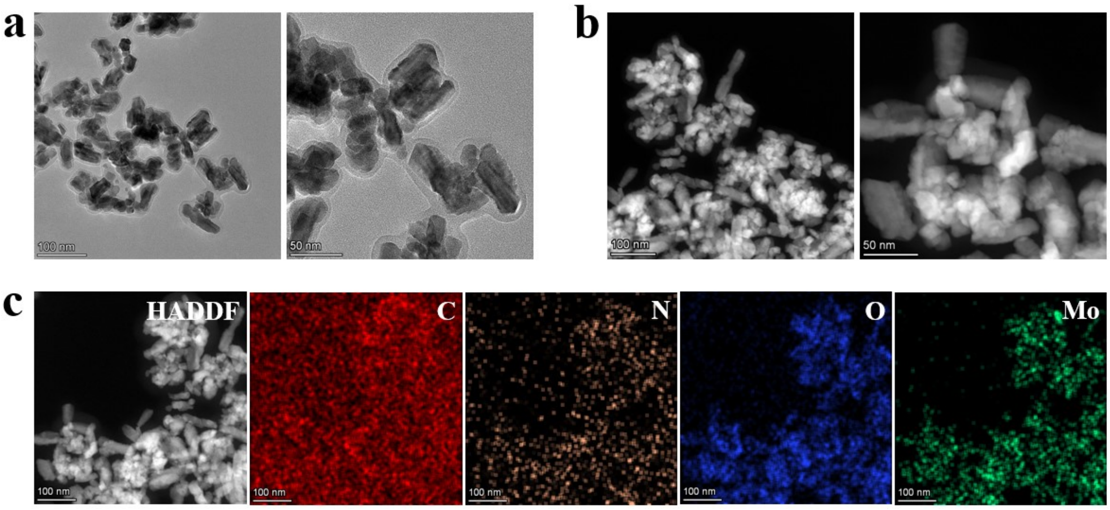

Fig. S22. (a) TEM images , (b) STEM images and (c) EDS mapping images of the MoO$_2$@NC.

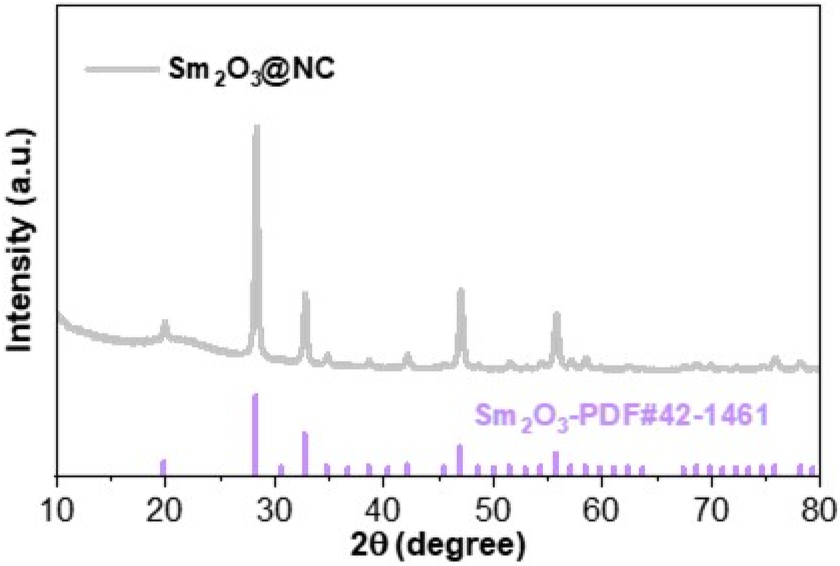

Fig. S23. The XRD patterns of the prepared Sm$_2$O$_3$@NC nanorods. The vertical lines represent for the standard peaks of Sm$_2$O$_3$ (PDF no. 42-1461).

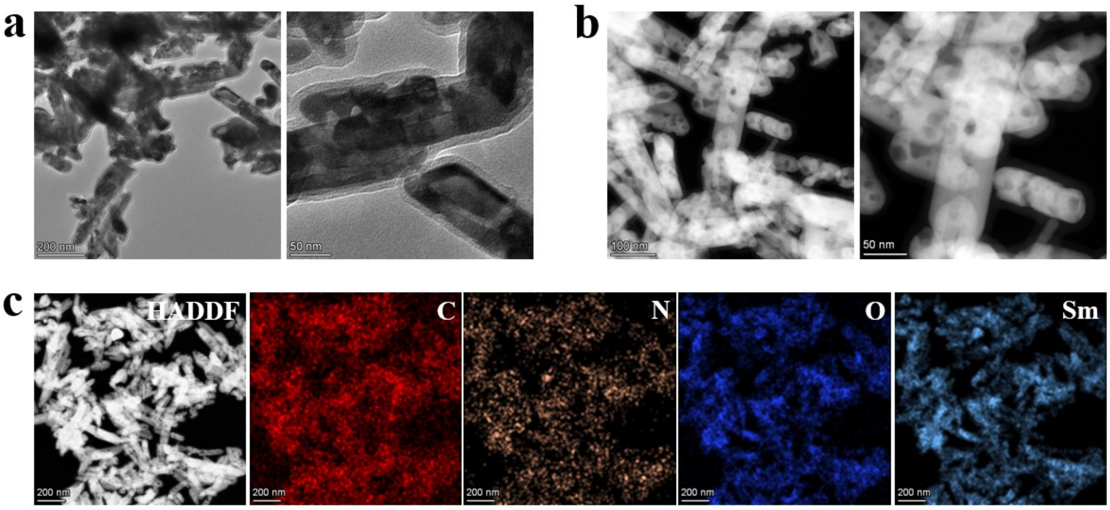

Fig. S24. (a) TEM images , (b) STEM images and (c) EDS mapping images of the Sm$_2$O$_3$@NC.

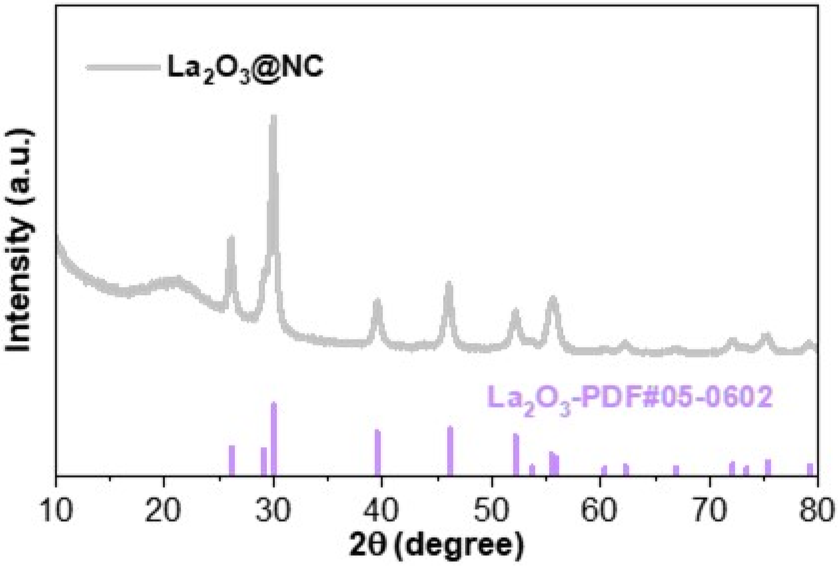

Fig. S25. The XRD patterns of the prepared La$_2$O$_3$@NC nanorods. The vertical lines represent for the standard peaks of La$_2$O$_3$ (PDF no. 05-0602).

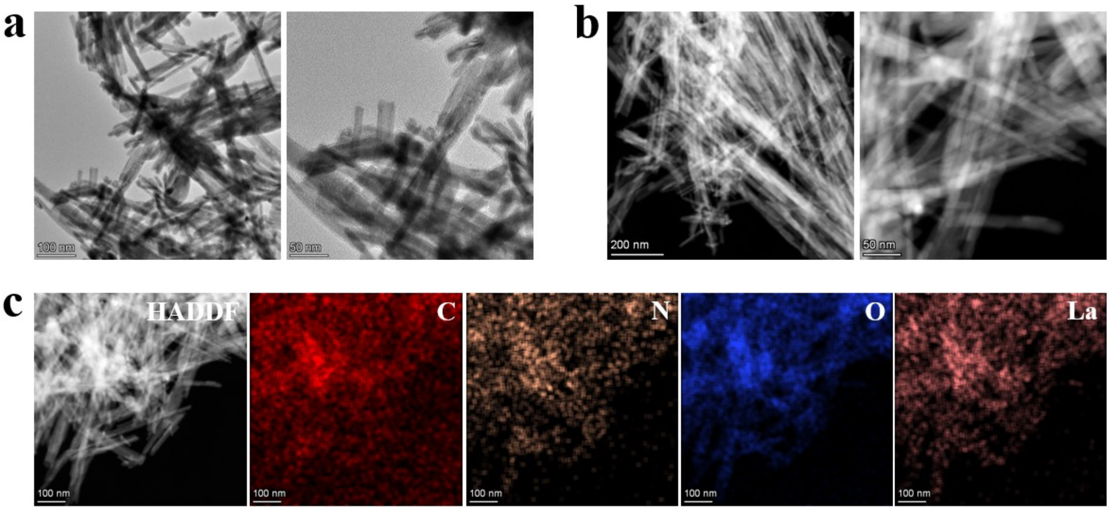

Fig. S26. (a) TEM images , (b) STEM images and (c) EDS mapping images of the La$_2$O$_3$@NC.

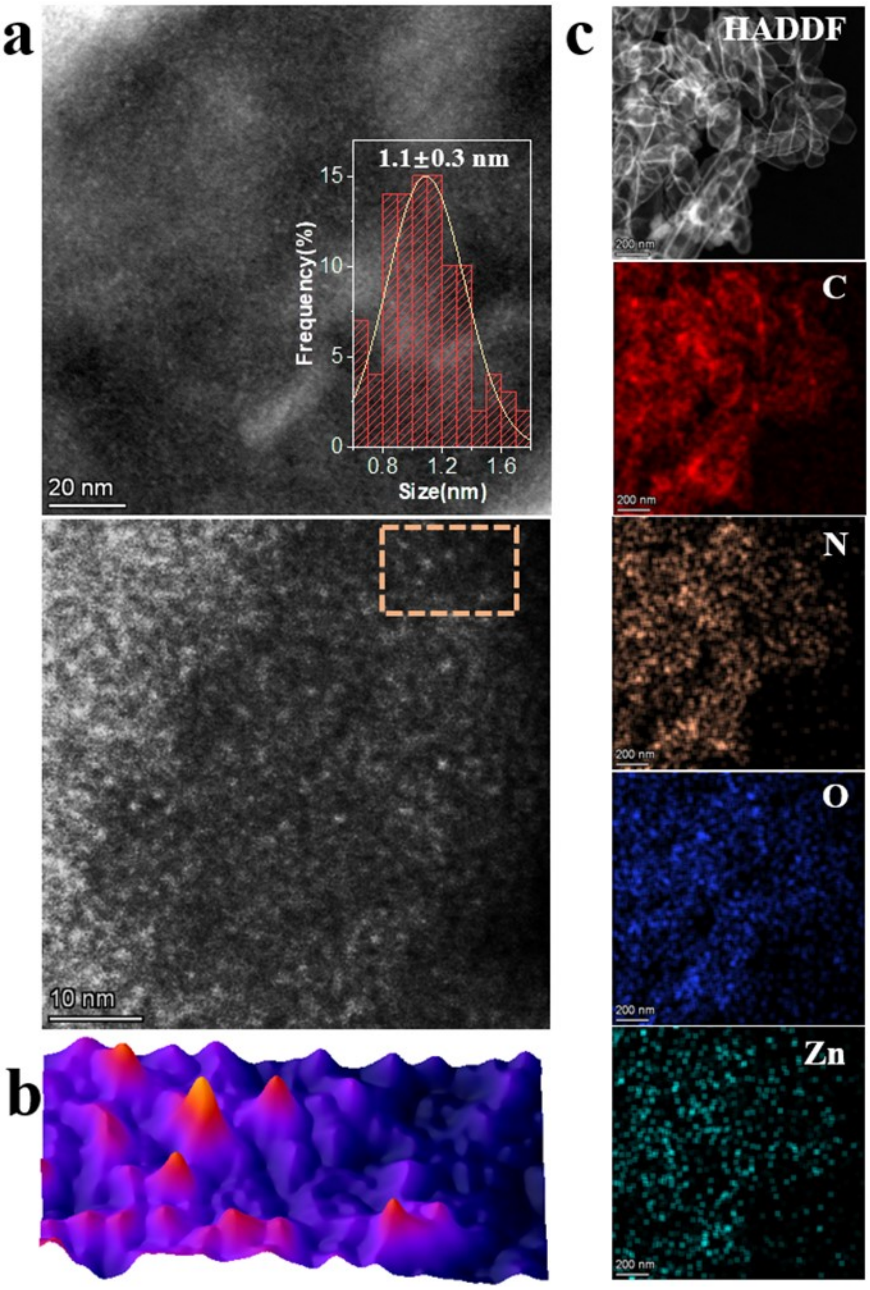

Fig. S27. (a) TEM images (inset is the size distribution of ZnO nanoclusters of ZnO/NC), (b) 3D surface tomographic image STEM images and (c) EDS mapping images of the of the ZnO/NC.

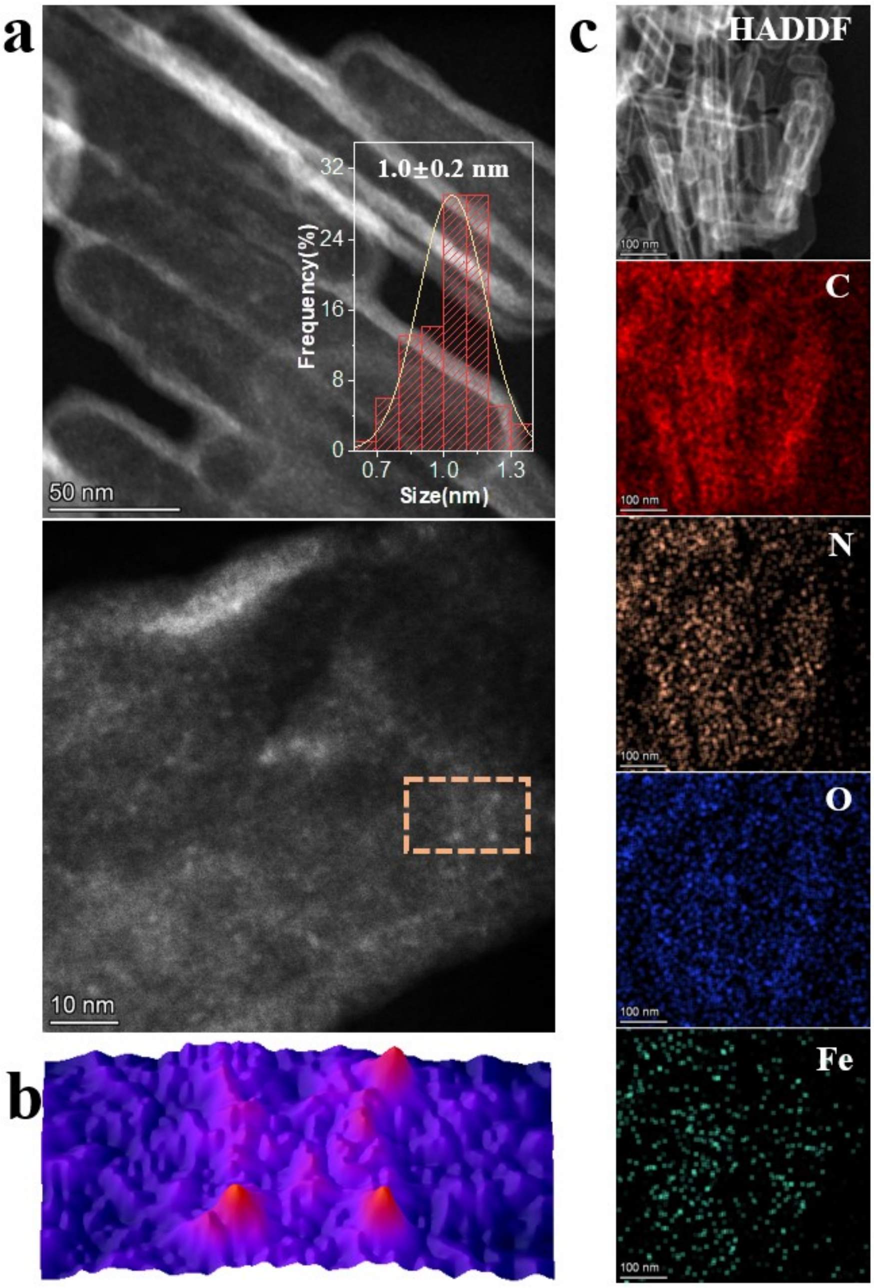

Fig. S28. (a) TEM images (inset is the size distribution of Fe_2O_3 nanoclusters of Fe_2O_3/NC), (b) 3D surface tomographic image STEM images and (c) EDS mapping images of the of the Fe_2O_3/NC.

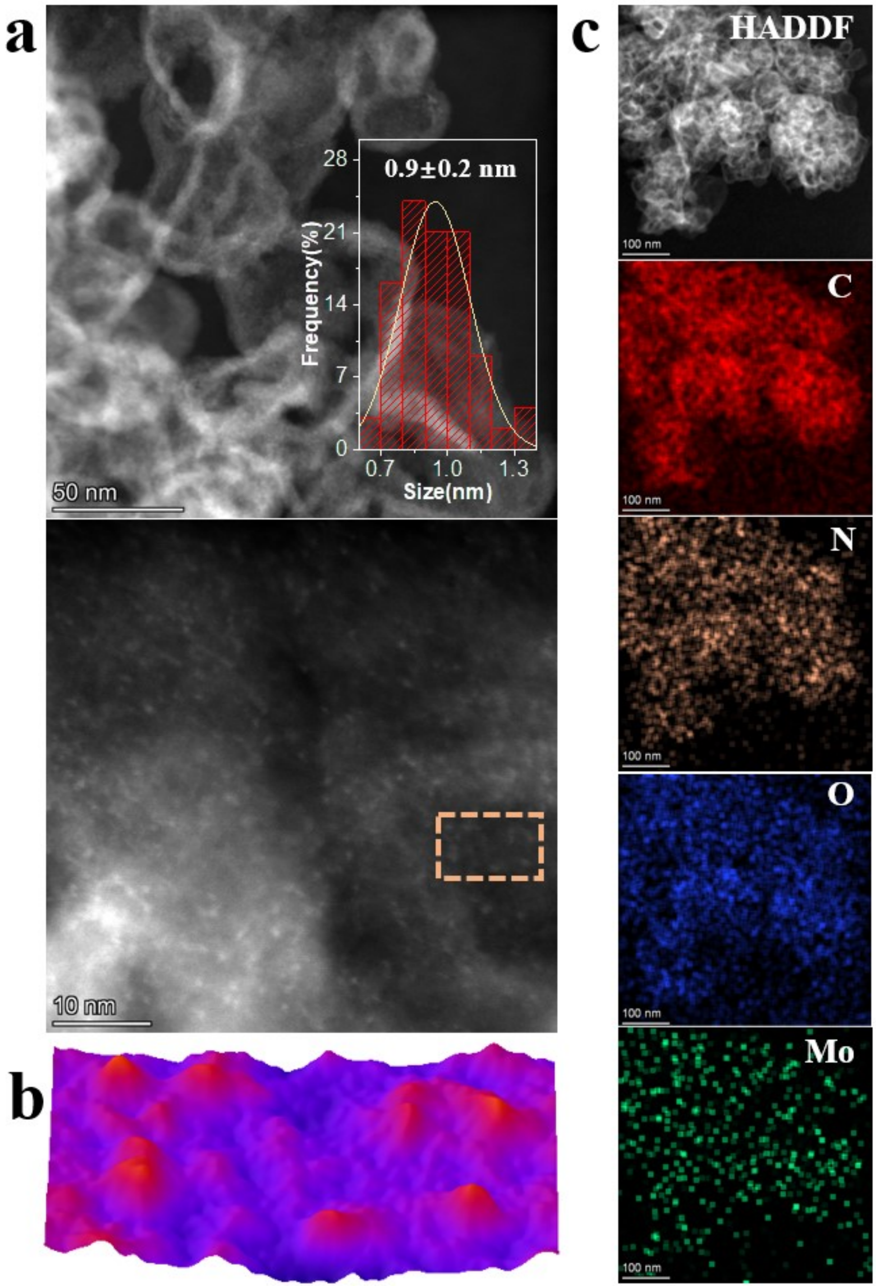

Fig. S29. (a) TEM images (inset is the size distribution of MoO_3 nanoclusters of MoO_3/NC), (b) 3D surface tomographic image STEM images and (c) EDS mapping images of the of the MoO_3/NC.

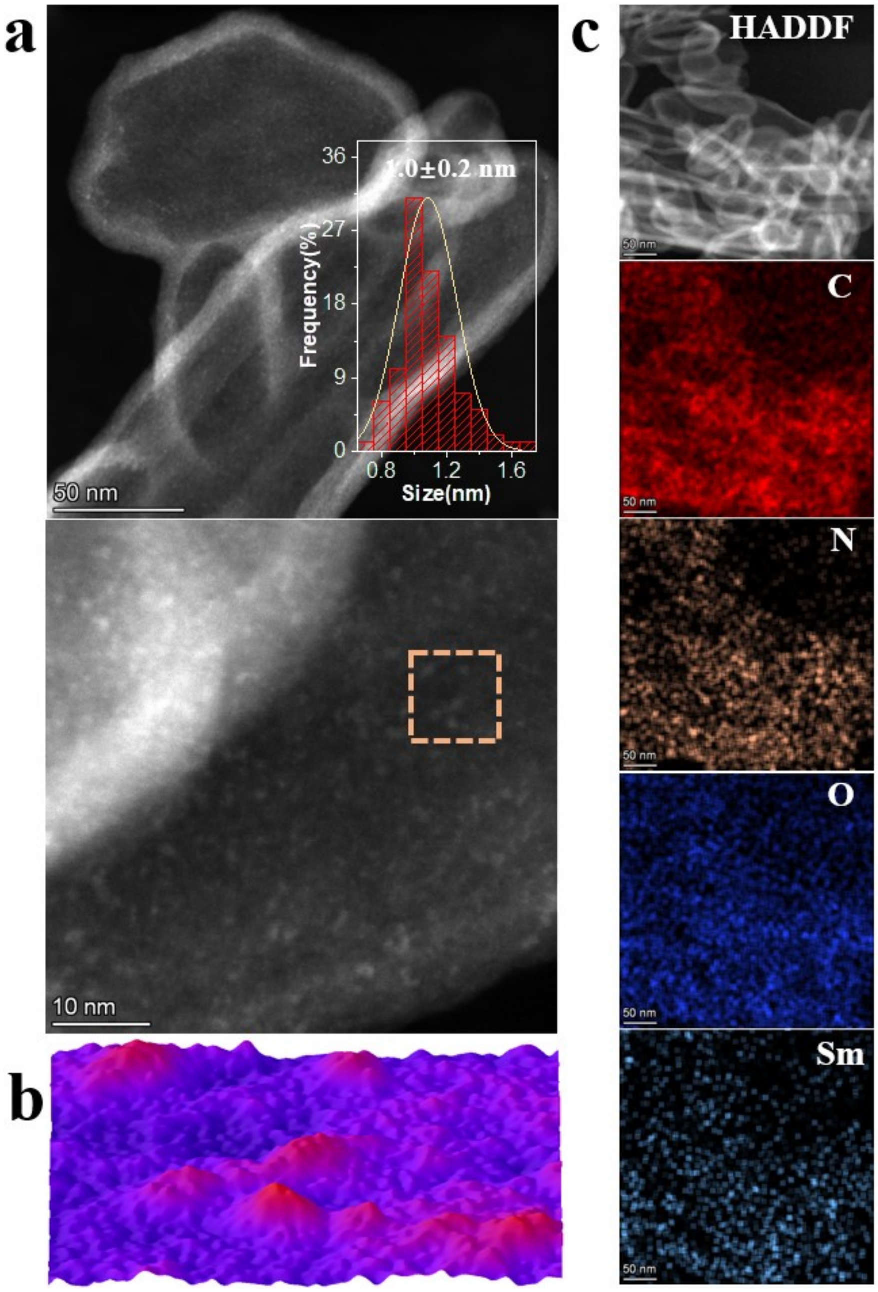

Fig. S30. (a) TEM images (inset is the size distribution of Sm_2O_3 nanoclusters of Sm_2O_3/NC), (b) 3D surface tomographic image STEM images and (c) EDS mapping images of the of the Sm_2O_3/NC.

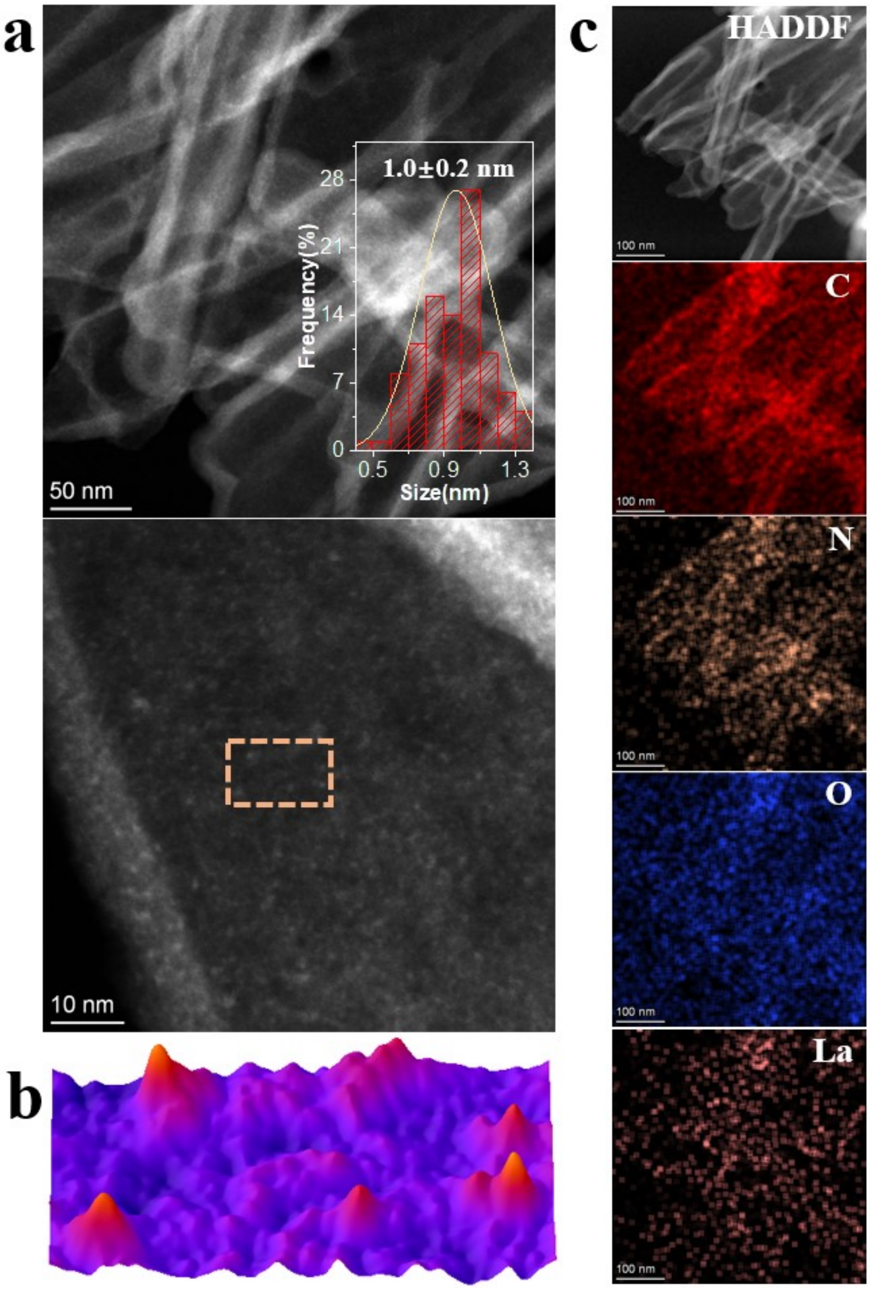

Fig. S31. (a) TEM images (inset is the size distribution of La_2O_3 nanoclusters of La_2O_3/NC), (b) 3D surface tomographic image STEM images and (c) EDS mapping images of the of the La_2O_3/NC.

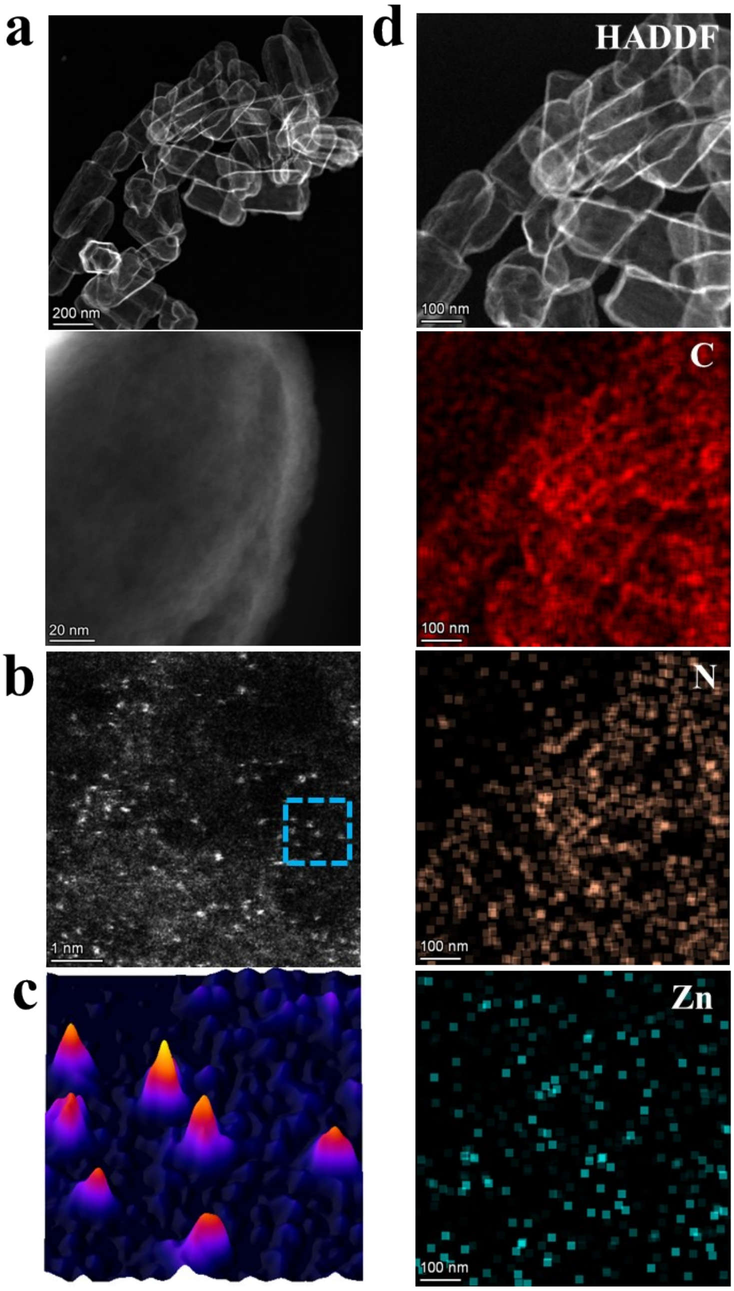

Fig. S32. (a)-(b) **S**TEM images, (c) 3D surface tomographic image, (d) EDS mapping images of the Zn_1/NC.

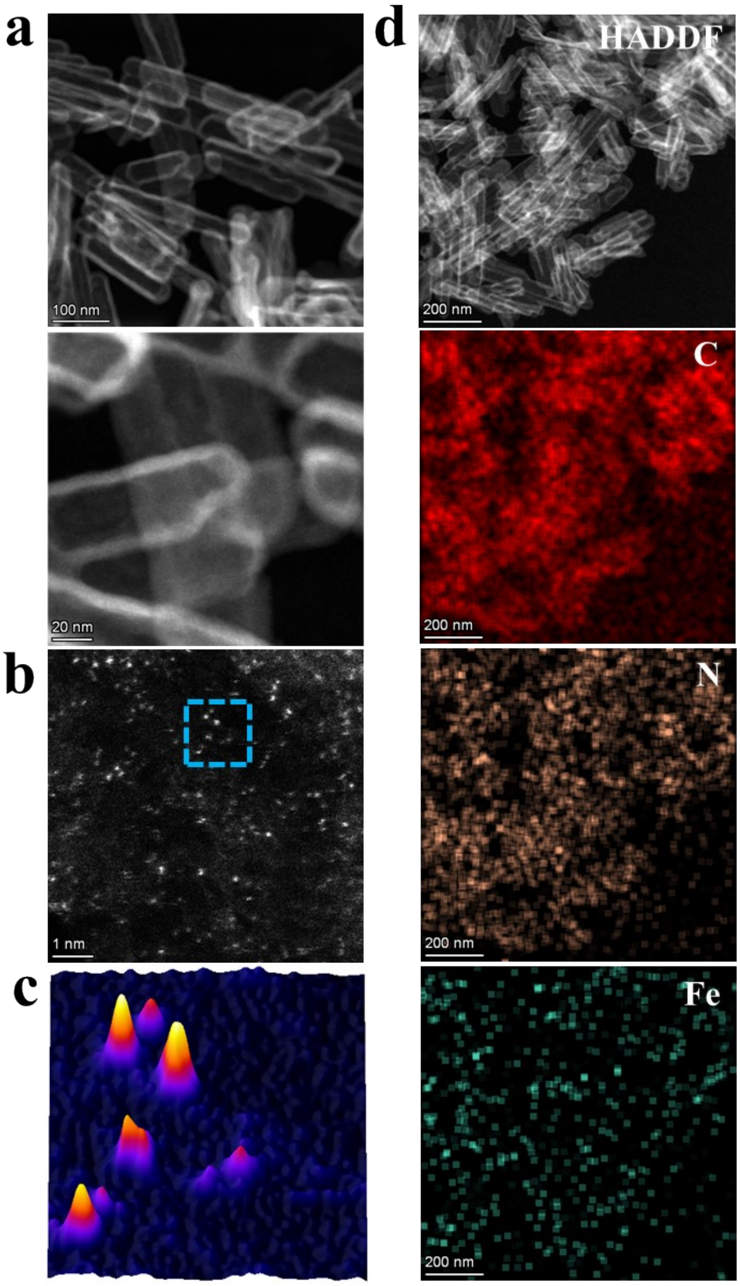

Fig. S33. (a)-(b) **S**TEM images, (c) 3D surface tomographic image, (d) EDS mapping images of the Fe$_1$/NC.

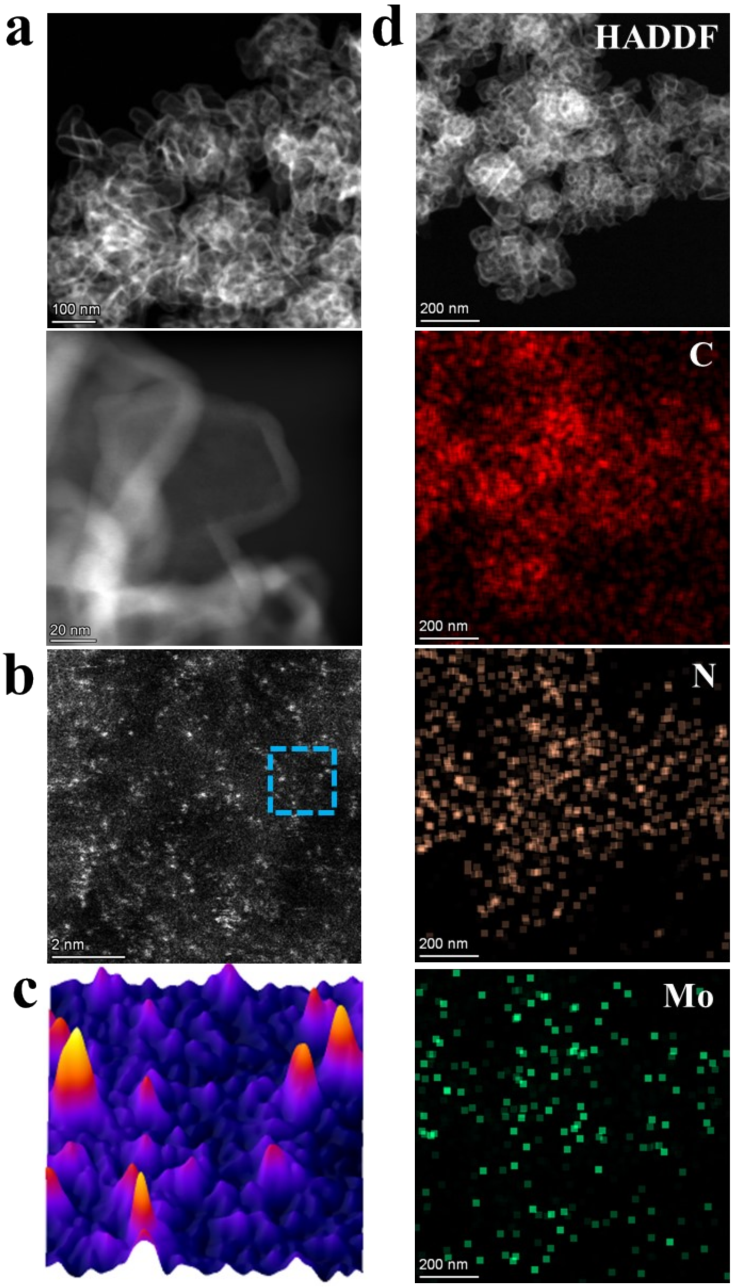

Fig. S34. (a)-(b) **S**TEM images, (c) 3D surface tomographic image, (d) EDS mapping images of the Mo_1/NC.

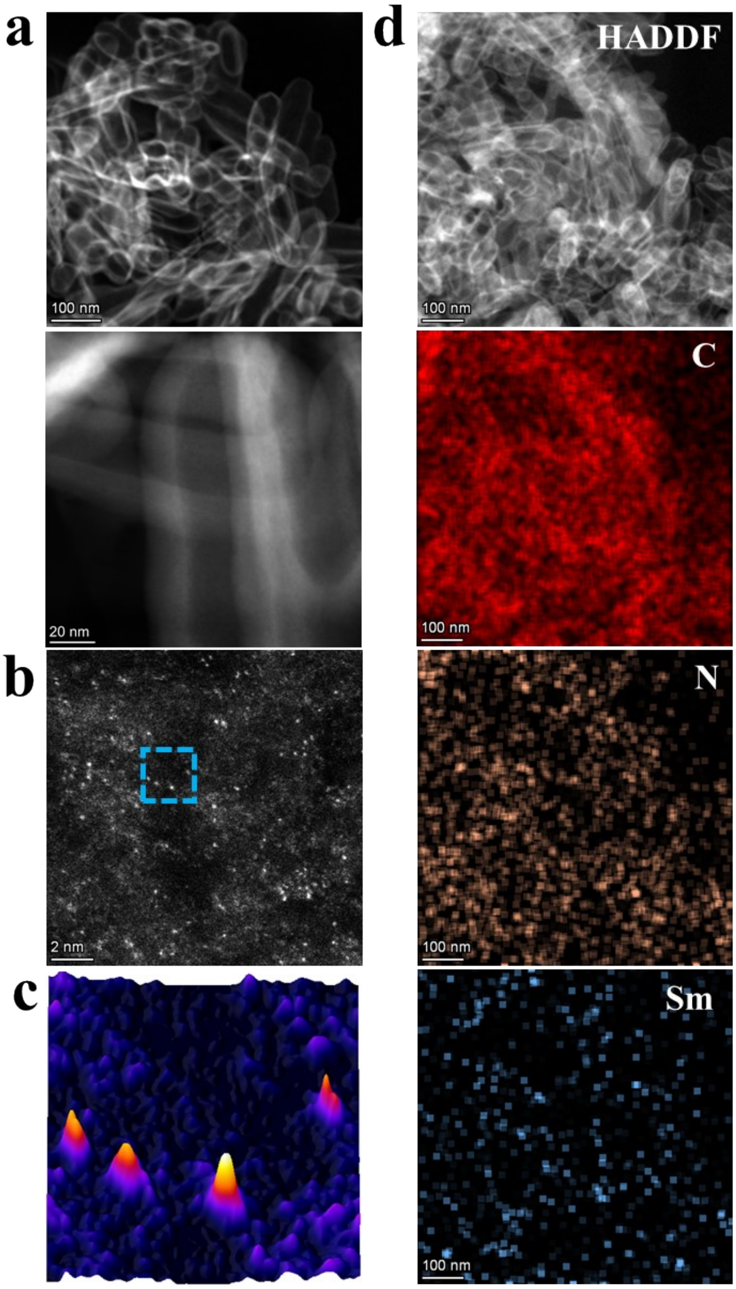

Fig. S35. (a)-(b) **S**TEM images, (c) 3D surface tomographic image, (d) EDS mapping images of the Sm_1/NC.

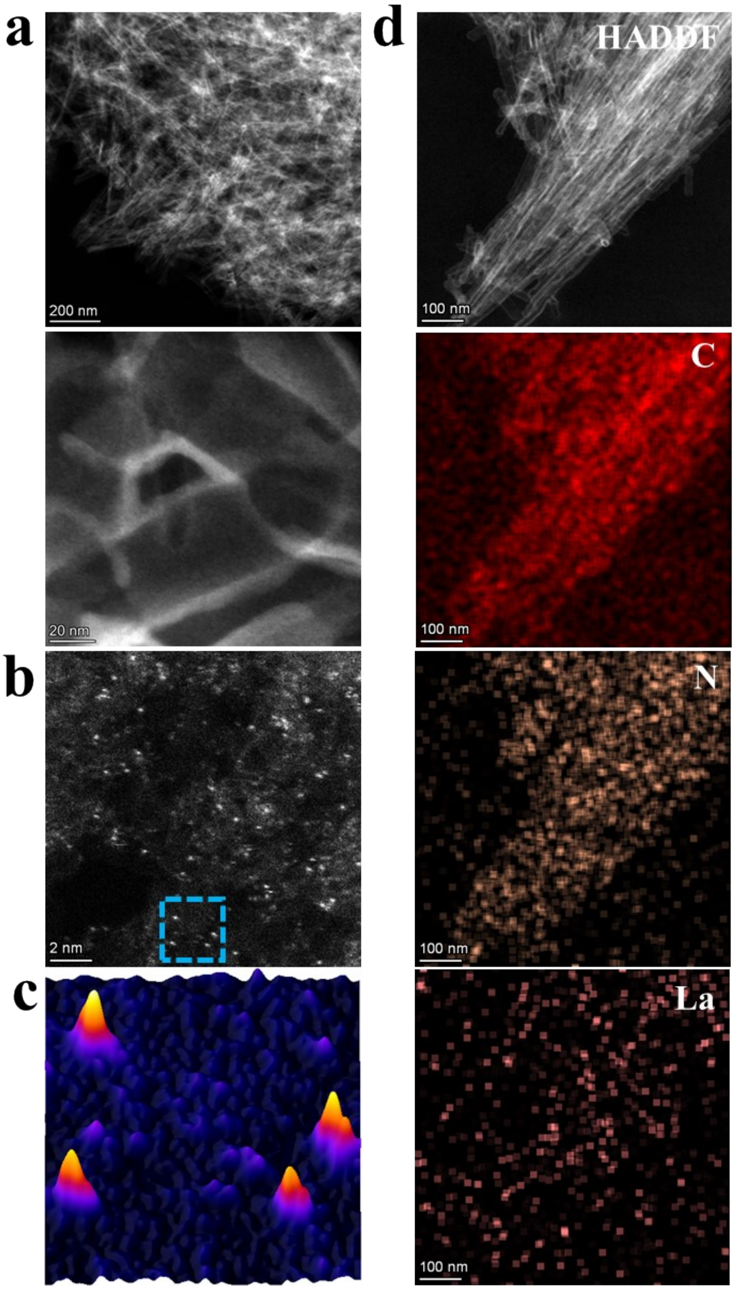

Fig. S36. (a)-(b) **S**TEM images, (c) 3D surface tomographic image, (d) EDS mapping images of the La_1/NC.

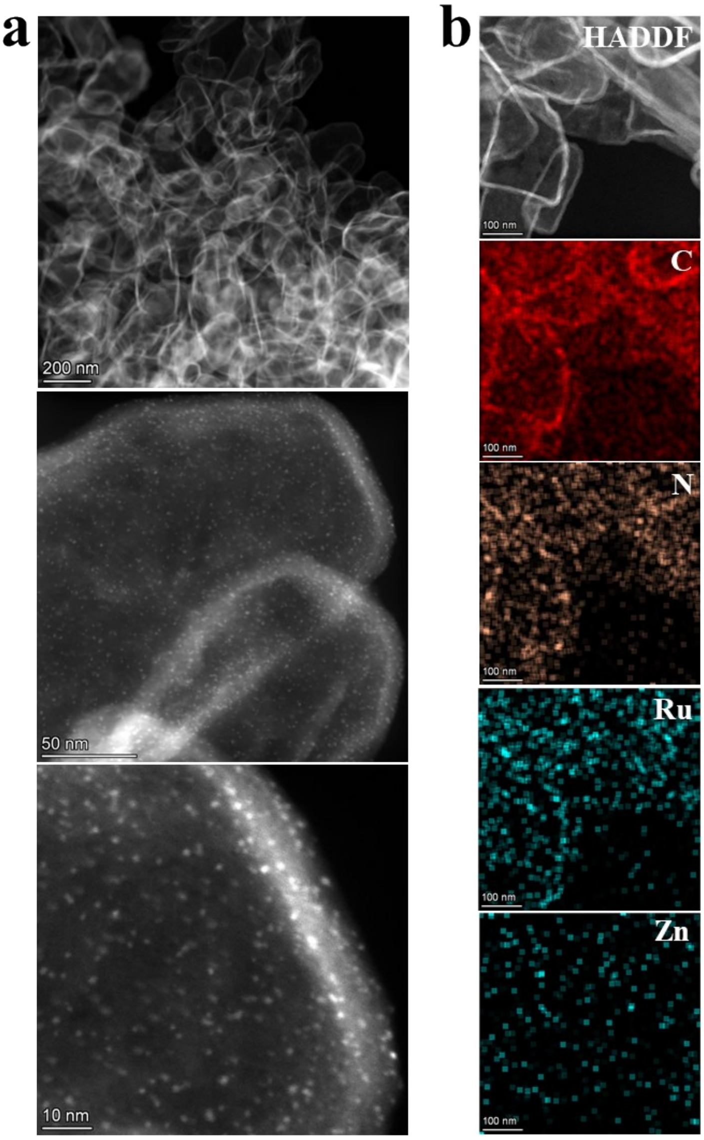

Fig. S37. (a) **S**TEM images, (b) EDS mapping images of the Zn_1-Ru_n/NC.

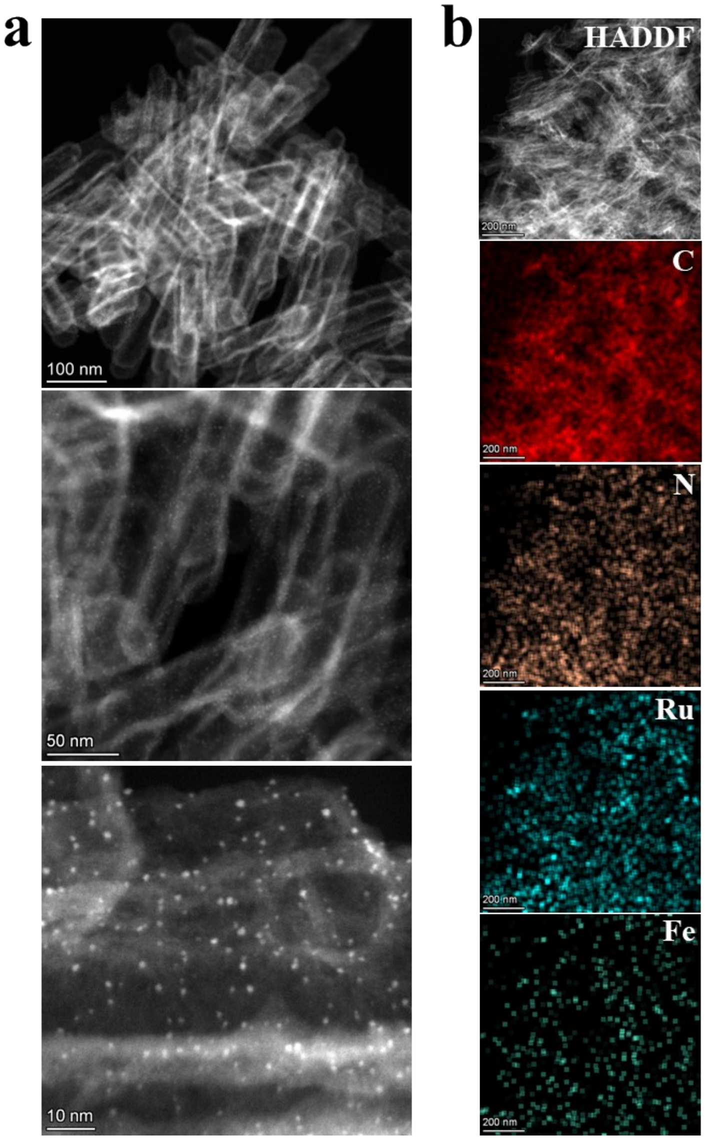

Fig. S38. (a) **S**TEM images, (b) EDS mapping images of the Fe_1-Ru_n/NC.

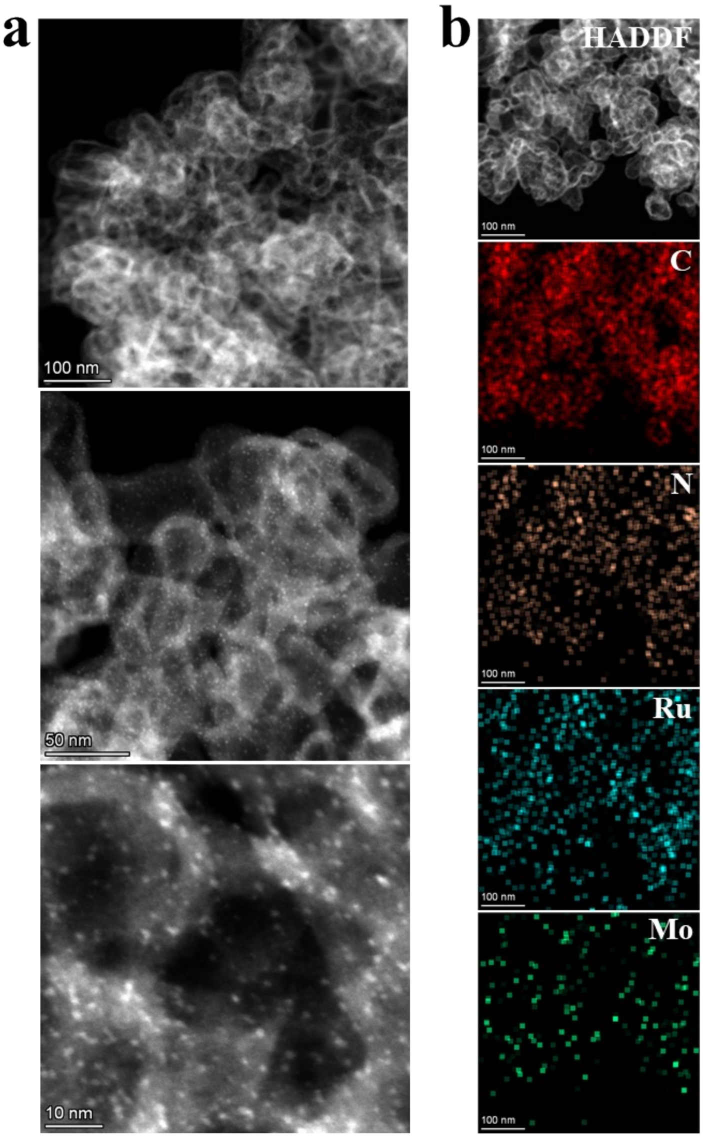

Fig. S39. (a) **S**TEM images, (b) EDS mapping images of the Mo$_1$-Ru$_n$/NC.

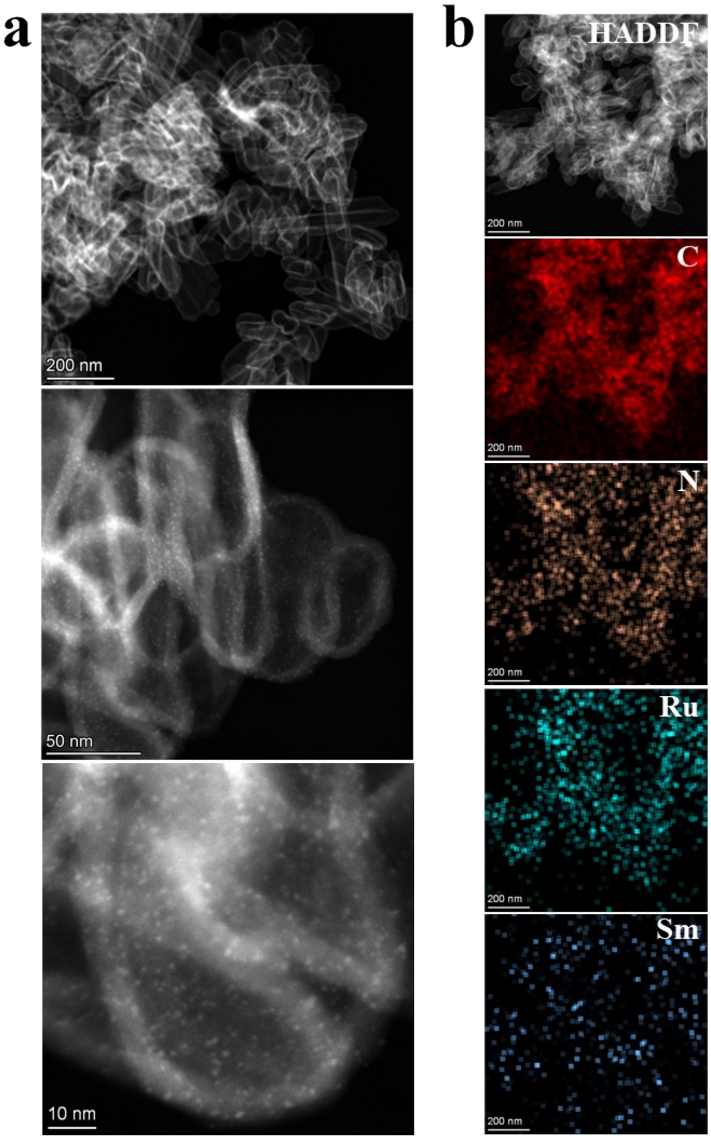

Fig. S40. (a) **S**TEM images, (b) EDS mapping images of the Sm_1-Ru_n/NC.

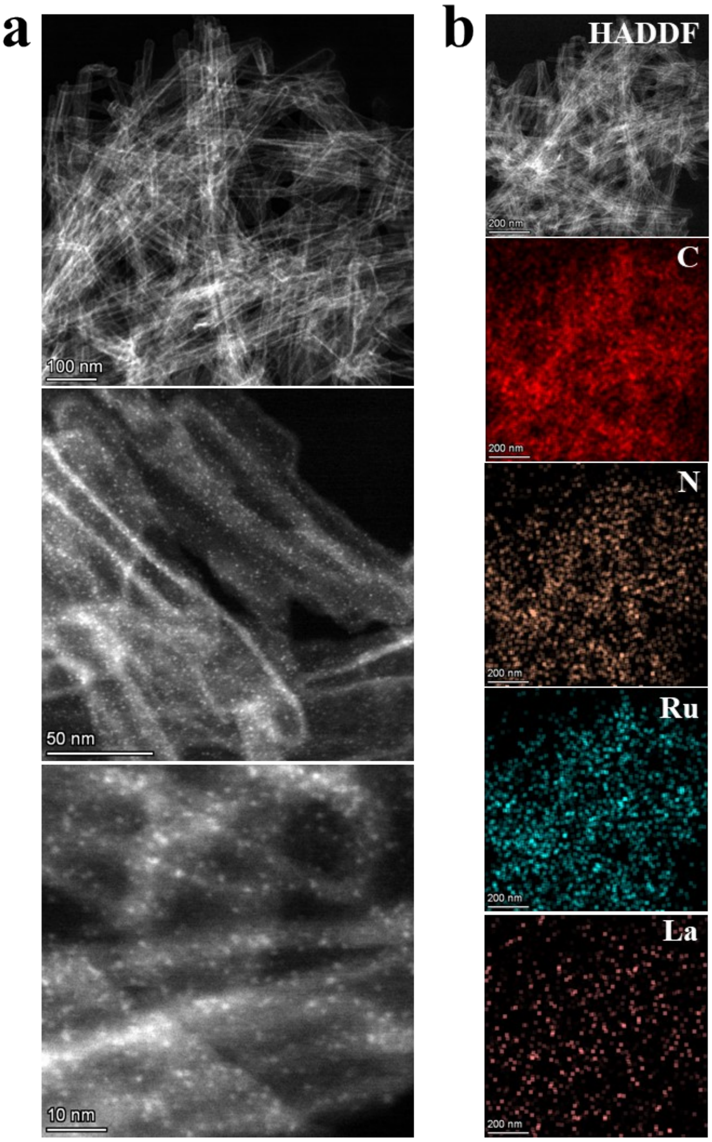

Fig. S41. (a) **S**TEM images, (b) EDS mapping images of the La_1-Ru_n/NC.

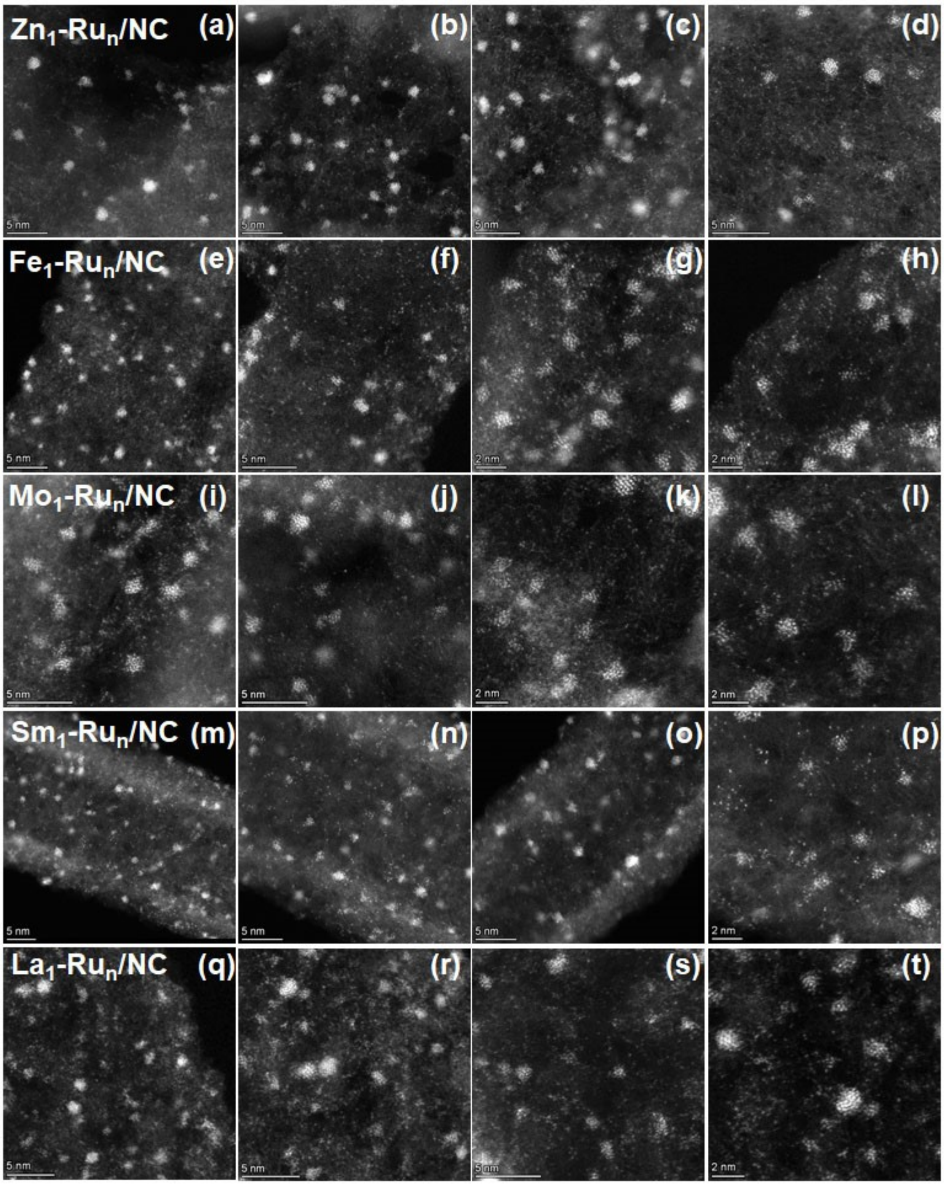

Fig. S42. (a)-(d) The atomic-resolution HAADF-STEM images of the Zn$_1$-Ru$_n$/NC catalyst. (e)-(h) The atomic-resolution HAADF-STEM images of the Fe$_1$-Ru$_n$/NC catalyst. (i)-(l) The atomic-resolution HAADF-STEM images of the Mo$_1$-Ru$_n$/NC catalyst. (m)-(p) The atomic-resolution HAADF-STEM images of the Sm$_1$-Ru$_n$/NC catalyst. (q)-(t) The atomic-resolution HAADF-STEM images of the La$_1$-Ru$_n$/NC catalyst.

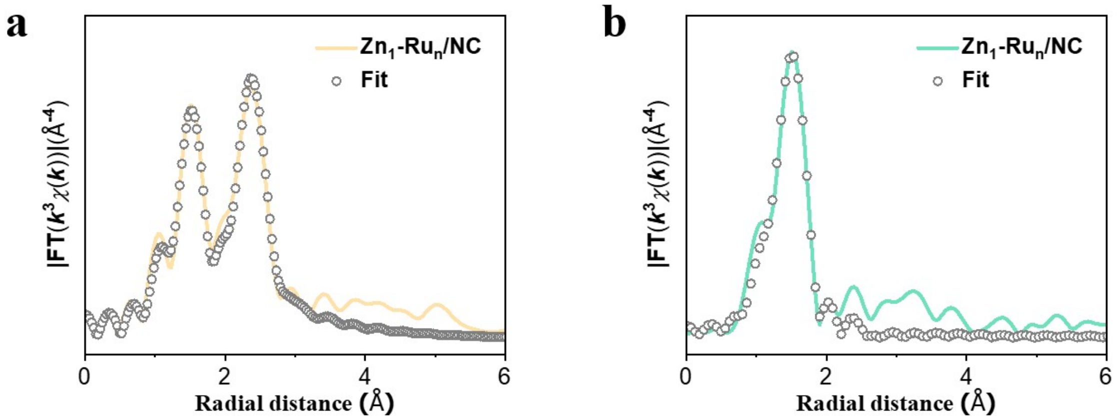

Fig. S43. (a) Ru K-edge, (b) Zn K-edge EXAFS fitting curves of Zn_1-Ru_n/NC shown in *R* space.

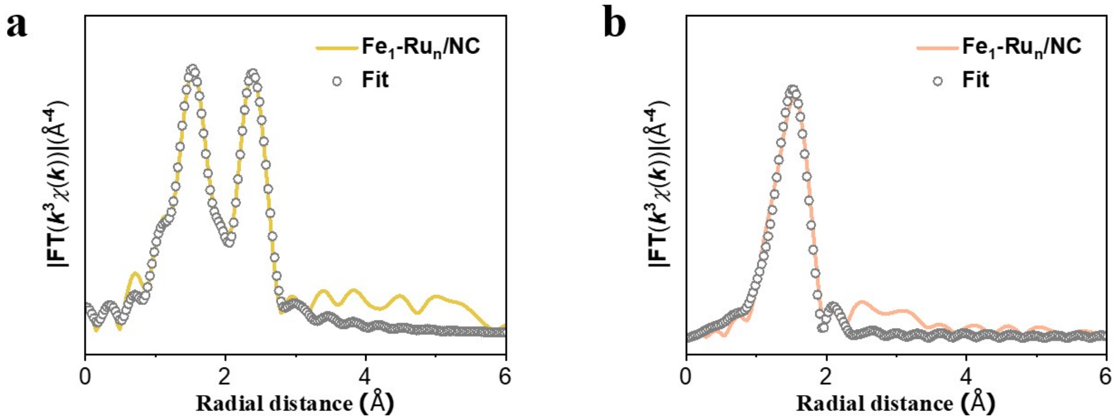

Fig. S44. (a) Ru K-edge, (b) Fe K-edge EXAFS fitting curves of Fe_1-Ru_n/NC shown in *R* space.

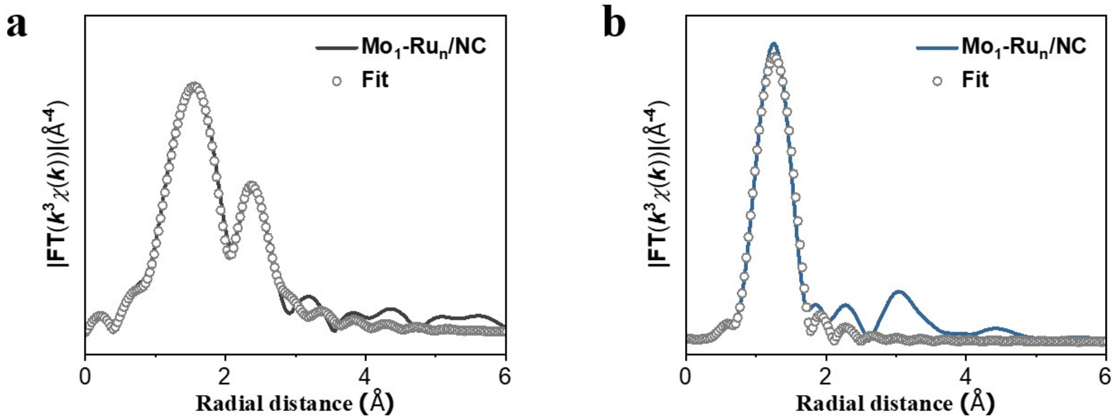

Fig. S45. (a) Ru K-edge, (b) Mo K-edge EXAFS fitting curves of Mo$_1$-Ru$_n$/NC shown in *R* space.

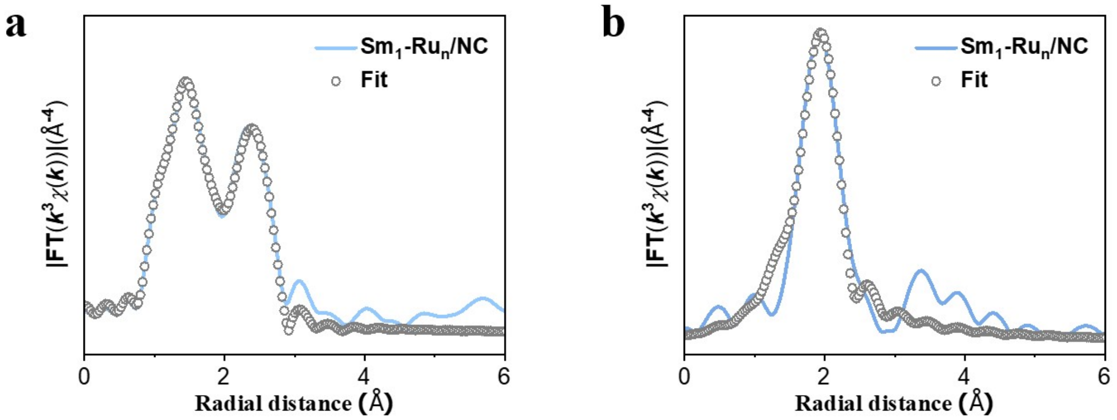

Fig. S46. (a) Ru K-edge, (b) Sm L$_3$-edge EXAFS fitting curves of Sm$_1$-Ru$_n$/NC shown in *R* space.

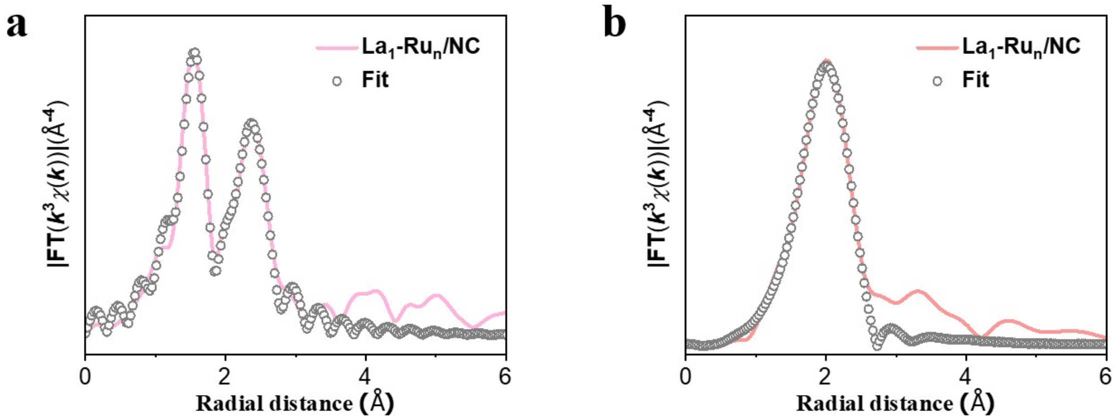

Fig. S47. (a) Ru K-edge, (b) La L_3-edge EXAFS fitting curves of La_1-Ru_n/NC shown in *R* space.

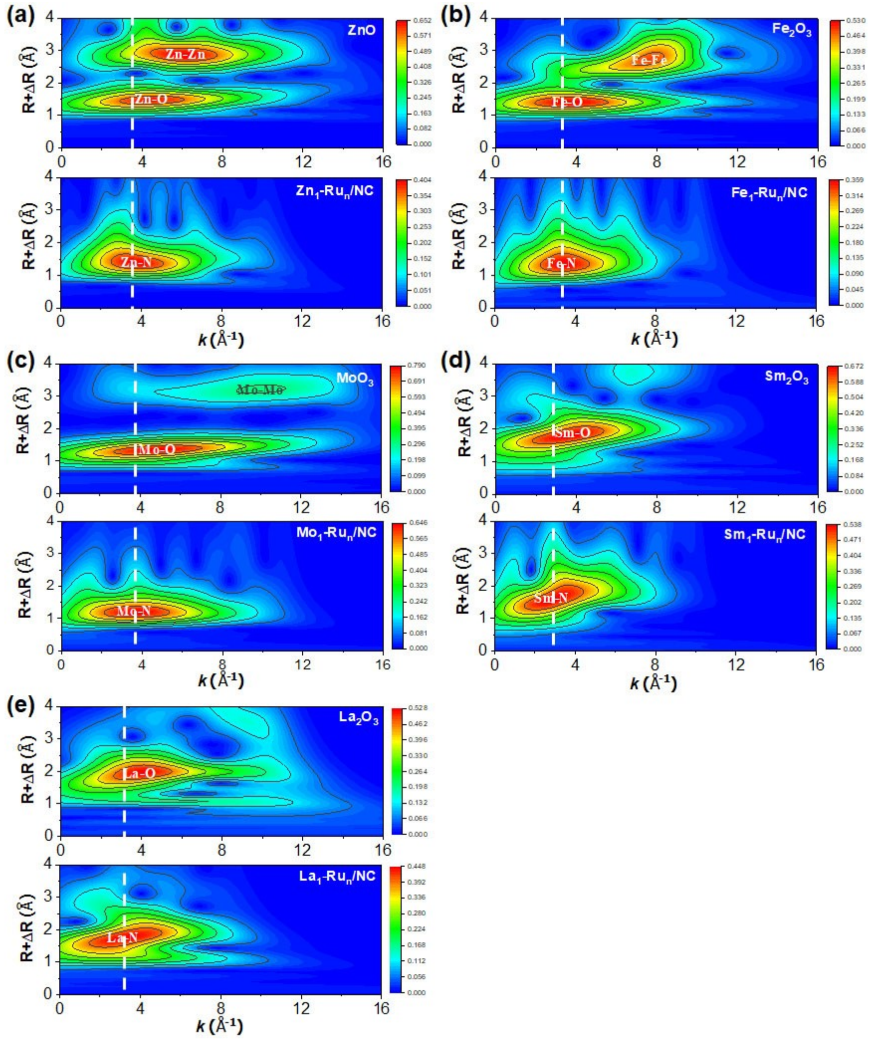

Fig. S48. (a) The wavelet transforms for the Zn K-edge EXAFS spectra of the Zn_1-Ru_n/NC catalyst and reference ZnO. (b) The wavelet transforms for the Fe K-edge EXAFS spectra of the Fe_1-Ru_n/NC catalyst and reference Fe_2O_3. (c) The wavelet transforms for the Mo K-edge EXAFS spectra of the Mo_1-Ru_n/NC catalyst and reference MoO_3. (d) The wavelet transforms for the Sm L-edge EXAFS spectra of the Sm_1-Ru_n/NC catalyst and reference Sm_2O_3. (e) The wavelet transforms for the La L-edge EXAFS spectra of the La_1-Ru_n/NC catalyst and reference La_2O_3.

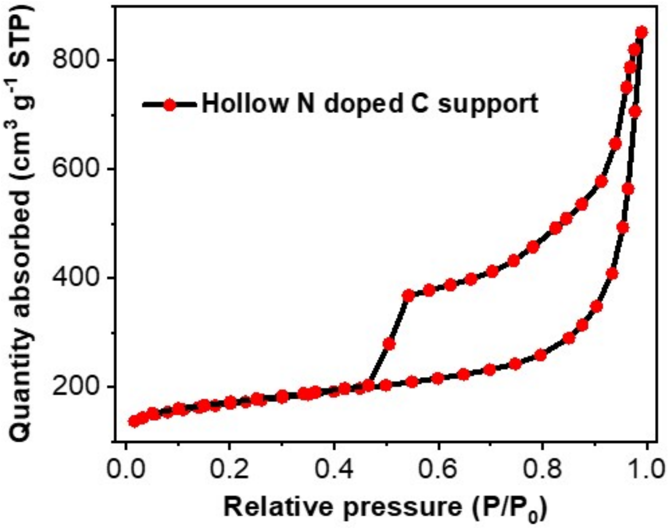

Fig. S49. The nitrogen adsorption–desorption isotherm profile of the dopamine-derived hollow-structured nitrogen-doped carbon support.

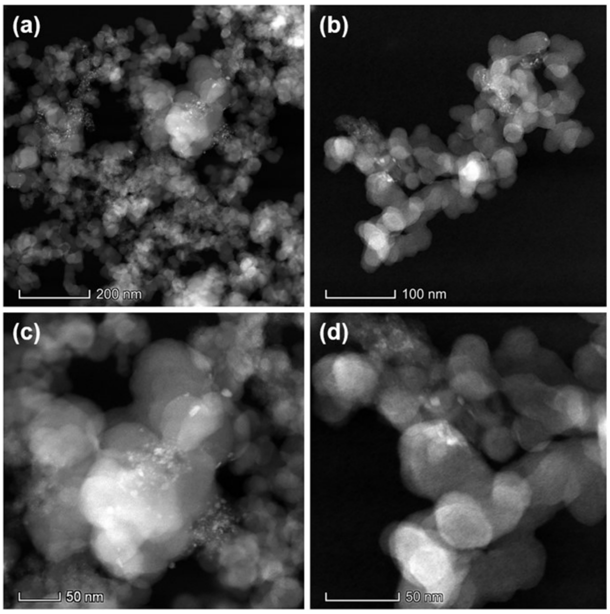

Fig. S50. (a)-(d) The HAADF-STEM images of the La/XC-72 catalyst with varied magnifications synthesized by loading the same amount of La onto the XC-72 as compared with the La_1-Ru_n/NC catalyst.

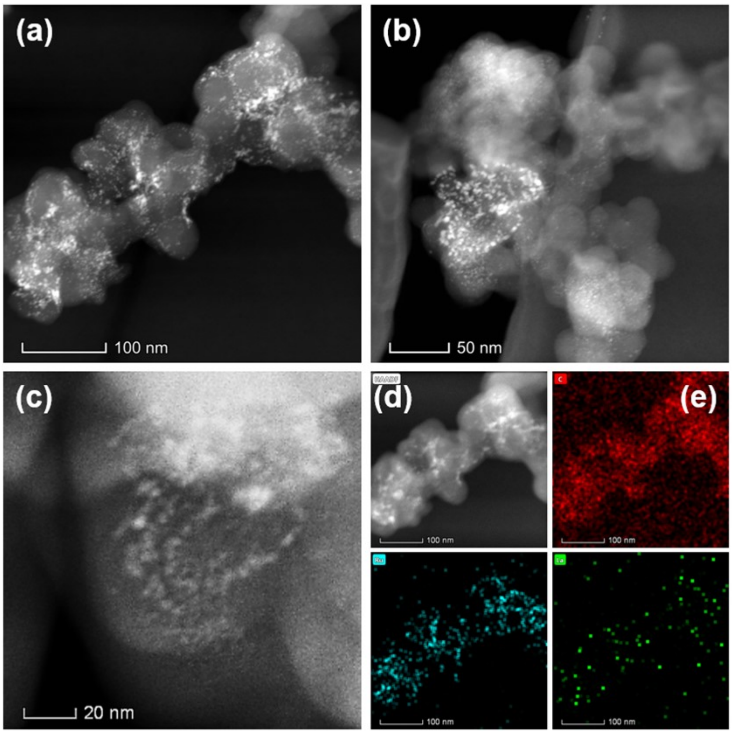

Fig. S51. (a)-(c) The HAADF-STEM images of the La-Ru/XC-72 catalyst with varied magnifications. (d) EDS mapping images of the synthesized La-Ru/XC-72 catalyst. To be noted that the Ru and La loadings in the La-Ru/XC-72 catalyst is kept the same to the La_1-Ru_n/NC catalyst.

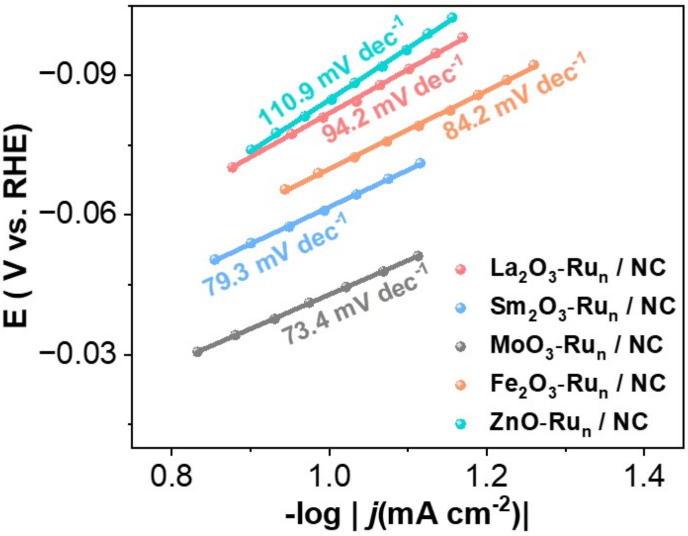

Fig. S52. The Tafel slopes of the M_xO_y-Ru_n/NC catalysts (M = Zn, Fe, Mo, Sm and La).

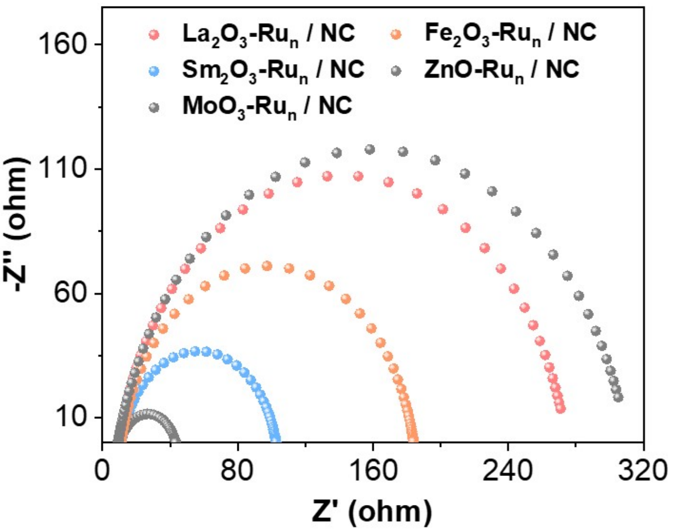

Fig. S53. Nyquist curves for the M_xO_y-Ru_n/NC catalysts (M = Zn, Fe, Mo, Sm and La).

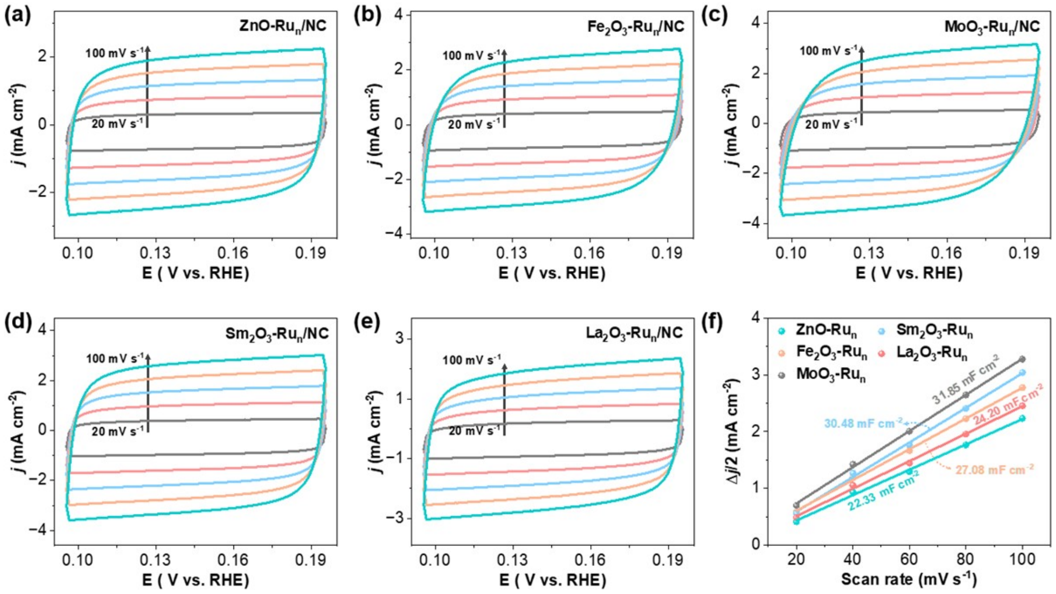

Fig. S54. (a)-(e) The CV curves measured in 1M KOH at different scan rates for the M_xO_y-Ru_n/NC catalysts (M=La, Sm, Mo, Fe, Zn), respectively. (f) Capacitive Δj as a function of scan rate of the M_1-Ru_n/NC catalysts (M=La, Sm, Mo, Fe, Zn), respectively.

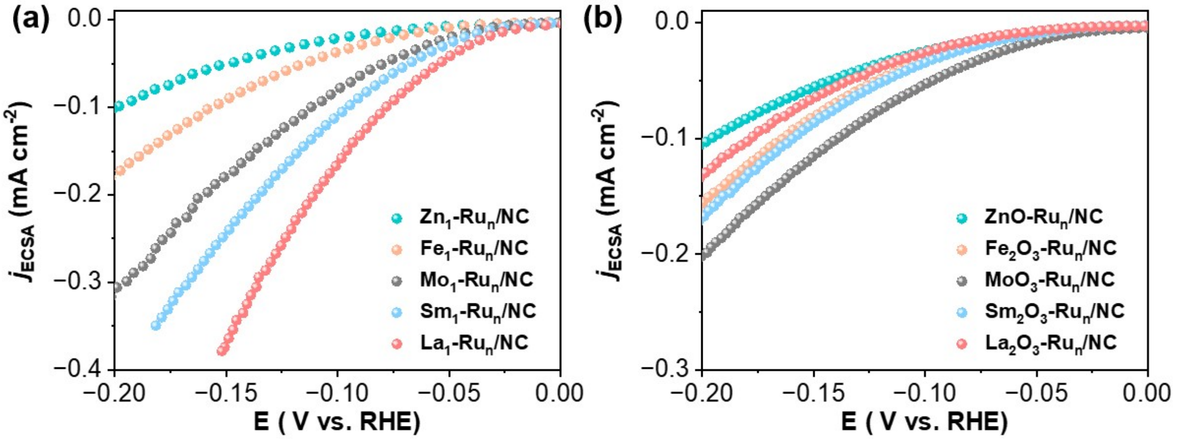

Fig. S55. The linear sweep voltammetry (LSV) curves of the (a) M_1-Ru_n/NC catalysts (M=La, Sm, Mo, Fe, Zn) and (b) M_xO_y-Ru_n/NC catalysts (M=La, Sm, Mo, Fe, Zn), acquired by normalizing the current densities of these catalysts to their ECSA values.

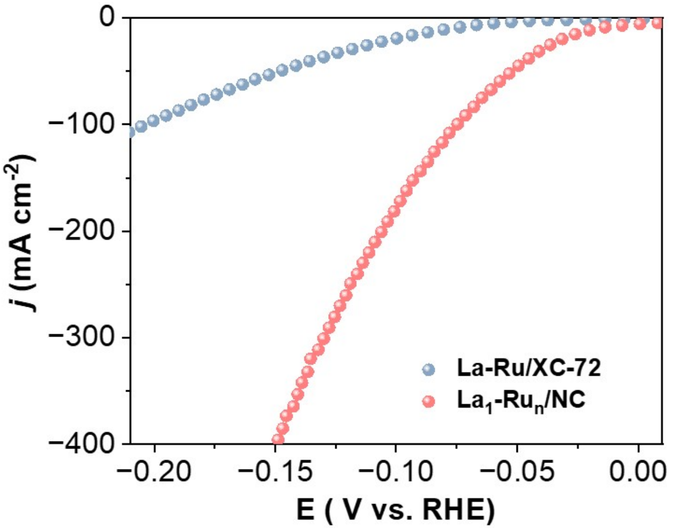

Fig. S56. The alkaline HER evaluations of the La1-Run/NC catalyst and the La-Ru/XC-72 catalyst conducted in 1M KOH.

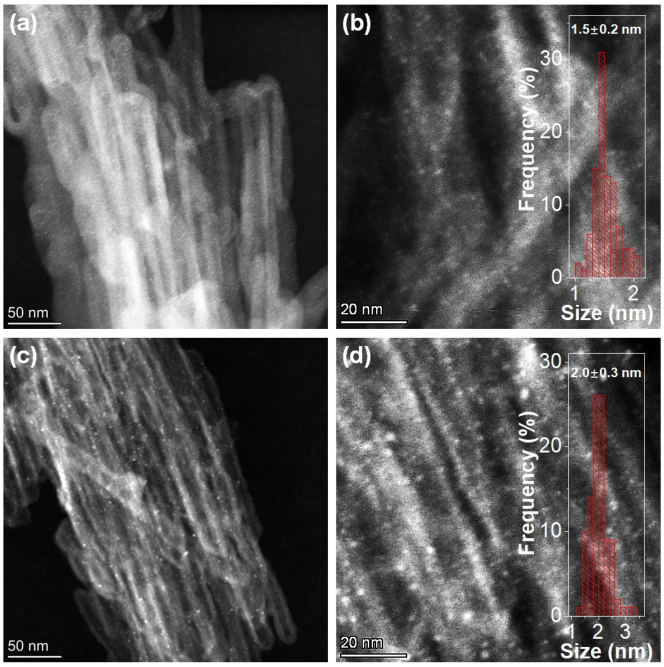

Fig. S57. (a)-(b) The HAADF-STEM images of the La_1-Ru_n/NC-R45 catalyst with varied magnifications. (c)-(d) The HAADF-STEM images of the La_1-Ru_n/NC-R55 catalyst with varied magnifications. The La_1-Ru_n/NC-R45 catalyst and the La_1-Ru_n/NC-R55 catalyst are obtained by reducing the Ru precursors at 450 °C and 550 °C, respectively.

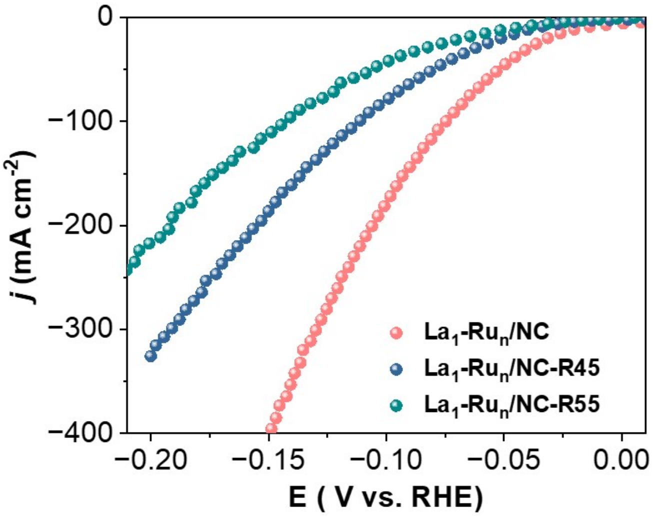

Fig. S58. Electrocatalytic alkaline HER evaluations of the La_1-Ru_n/NC catalyst, the La_1-Ru_n/NC-R45 catalyst and the La_1-Ru_n/NC-R55 catalyst, respectively, performed in 1M KOH.

s

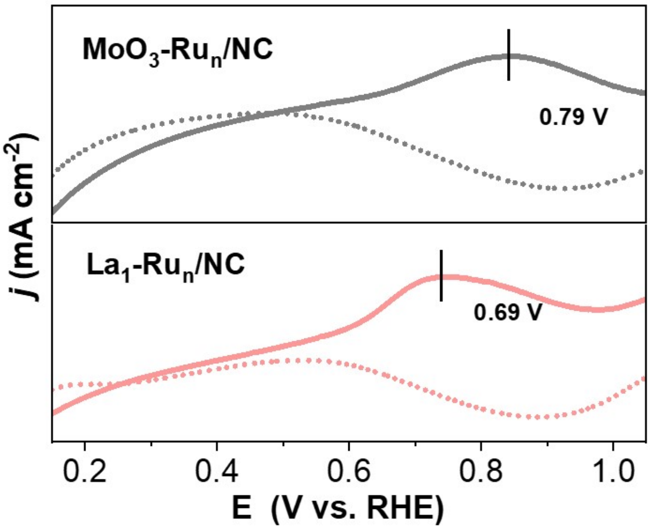

Fig. S59. The CO stripping curves of the La$_1$-Ru$_n$/NC catalyst, and the MoO$_3$-Ru$_n$/NC catalyst, respectively.

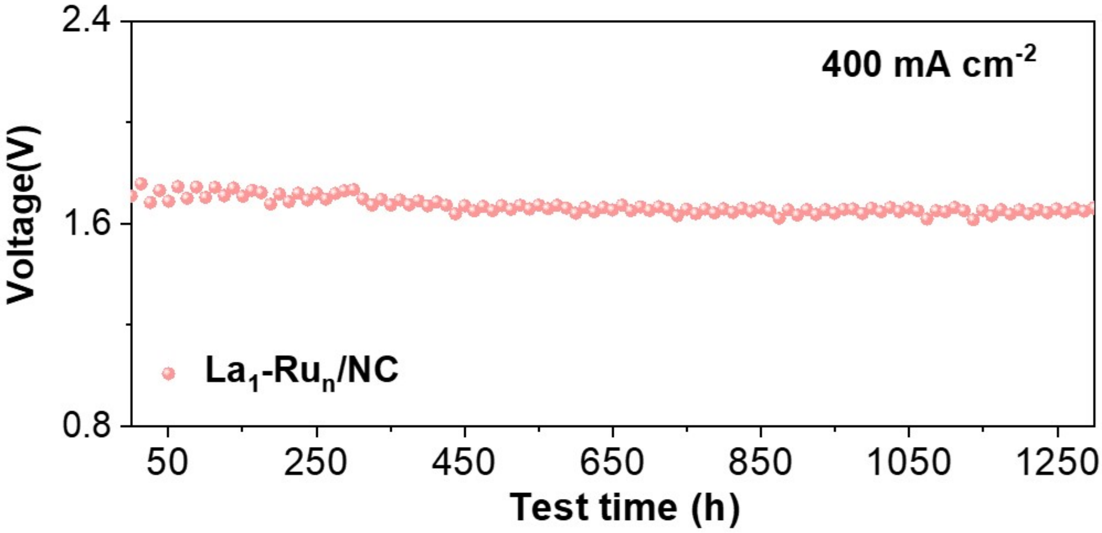

Fig. S60. The durability test of the NF||La$_1$-Ru$_n$/NC measured at the current density output of 400 mA·cm^{-2} at 80 °C in 1M KOH.

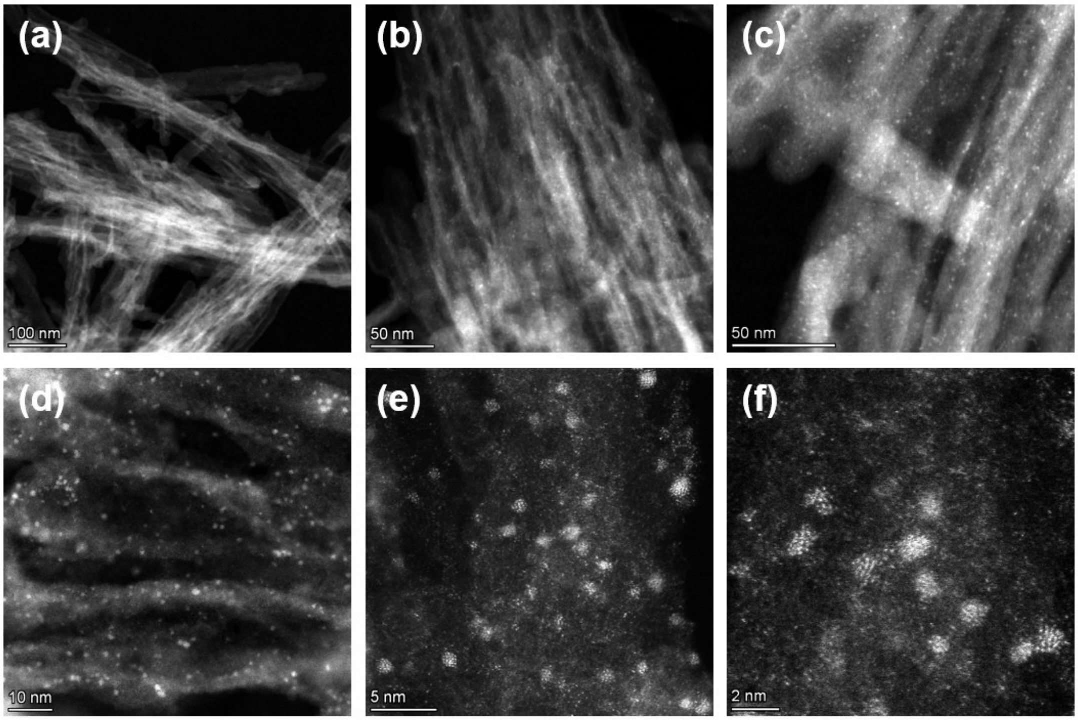

Fig. S61. (a)-(f) STEM images of the post-reaction La_1-Ru_n/NC catalyst after the stability test performed at 1000 mA·cm^{-2}.

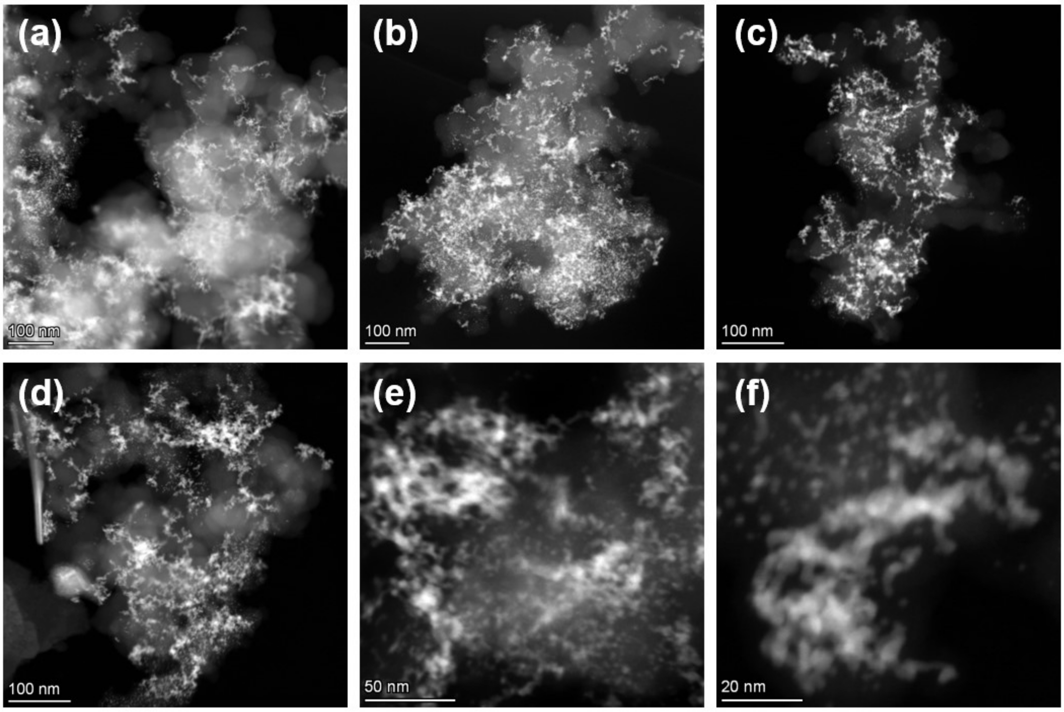

Fig. S62. (a)-(f) STEM images of the post-reaction 20 wt.% Pt/C catalyst after the stability test performed at 1000 mA·cm^{-2}.

Supplementary Tables

Table S1. The EXAFS fitting results of the M$_1$-Ru$_n$/NC (M= Zn, Fe, Mo, Sm, La) catalysts.

Sample	**path**	**CN**	**R (Å)**	***σ*^{2} (Å^2)**	**ΔE$_0$ (eV)**	**R factor**	**S$_0$^{2}**
Ru foil	Ru-Ru	12	2.68	0.0042	-4.5	0.0048	0.906
Zn$_1$-Ru$_n$/NC	Ru-N	4.4	2.05	0.0085	-2.6	0.0078	0.876
	Ru-Ru	2.3	2.69	0.0040	-2.6		
	Zn-N	3.7	2.00	0.0067	-1.5	0.0038	0.917
Fe$_1$-Ru$_n$/NC	Ru-N	4.1	2.07	0.0101	-1.3	0.0023	0.876
	Ru-Ru	1.9	2.70	0.0068	-1.3		
	Fe-N	4.2	2.03	0.0095	2.2	0.0120	0.798
Mo$_1$-Ru$_n$/NC	Ru-N	4.1	2.05	0.0067	-0.8	0.0120	0.862
	Ru-Ru	1.9	2.70	0.0025	-0.8		
	Mo-N	4.2	1.79	0.0040	5.9	0.0053	0.821
Sm$_1$-Ru$_n$/NC	Ru-N	3.7	2.02	0.0111	-2.4	0.0275	0.926
	Ru-Ru	2.3	2.69	0.0094	-2.4		
	Sm-N	6.3	2.43	0.0117	-0.7	0.0133	0.900
La$_1$-Ru$_n$/NC	Ru-N	4.0	2.06	0.0068	-2.4	0.0082	0.906
	Ru-Ru	2.1	2.68	0.0057	8.4		
	La-N	5.8	2.63	0.0097	9.3	0.0101	0.900

CN is the coordination number; *R* is the distance between absorber and backscatter atoms; σ^2 is the Debye-Waller factor value; ΔE_0 is the inner potential correction; *R* factor indicates the goodness of the fit. A reasonable range of the structural parameters fitting parameters obtained by EXAFS spectroscopy are estimated as CN ± 20%; R ± 1%; σ^2 ± 20%; ΔE_0 ± 20%. S_0^2 was fixed between 0.700 and 1.000 during the data fitting.

Table S2. The output current density, turnover frequency (TOF), Faradaic efficiency (FE) and Ru loadings between the La_1-Ru_n/NC catalyst and previously reported Ru-based catalyst measured at -0.1 V vs. RHE for alkaline HER in 1M KOH electrolyte.

Sample	***j*** **($mA \cdot cm^{-2}$)**	**Ru loading (wt.%)**	**TOF (s^{-1})**	**FE (%)**	**Reference**
La_1-Ru_n/NC	-178	3.07	44.7	99.3	This work
PtRu/CNT@CeO_{2-x}	-158	Pt-4.68 Ru-2.61	-	-	*J Am Chem Soc* **146**, 21453-21465 (2024).
Ru/Na^+, K^+-PC	-158	6.02	8.41	99.1	*Nano Res* **16**, 8836-8844 (2023).
RuP/PNPC	-154	29.0	-	98.2	*SusMat.* **4**, 166-177 (2024).
HEANC/C	-154	14.5	-	-	*Adv Mater* **36**, 2309715 (2024).
Ru-a-CoNi	-145	2.47	-	98.3	*Angew Chem, Int Ed.* **134**, e202114160 (2022).
Ru/S-Ni_2P	-127	-	1.03	-	*J Mater Chem A* **9**, 15648-15653 (2021).
$LaCeO_x$@NGr/Ru_1	-119	1.5	-	-	*Appl Catal, B.* **343**, 123452 (2024).
RuBi SAA/Bi@OG	-114	32.3	25.7	-	*Angew Chem, Int Ed.* **62**, e202300879 (2023).
Ru/3DLNC-500	104	1.8	-	-	*ACS Sustainable Chem Eng* **12**,

					5319-5331 (2024).
Ru-NiO/CNTs	-100	0.94	-	-	*Chem Eng J.* **472**, 144922 (2023).
Ru/NC	-97	5.83	-	-	*Adv Mater* **35**, 2301133 (2023).
Ru SAs/WCx	ca. -89	1.26	-	-	*J Am Chem Soc* **146**, 4883-4891 (2024).
Cu-Ru/RuSe$_2$ NSs/C	ca. -85	-	0.88	-	*Adv Mater* **35**, 2300980 (2023).
Ru/ac-CeO$_{2-\delta}$	-82	-	-	-	*Angew Chem, Int Ed.* **136**, e202317622 (2024).
Ru$_{0.18}$Ni-LDH-A	-77	19.9	3.68	-	*Small.* **20**, 2311076 (2024).
Ru/α-MoC	-72.4	7.65	39.2	-	*Appl Catal, B.* **318**, 121867 (2022).
RuPd/C	-69.7	20	-	-	*J Mater Chem A* **11**, 13783-13792 (2023).
Ru/P-TiO$_2$	ca. -69	-	-	-	*Angew Chem, Int Ed.* **134**, e202212196 (2022).
Ru/d-NiFe LDH	-69	2.06	-	99.8	*Adv Energy Mater* **14**, 2400059 (2024).
Ru/RuS$_2$@h-NSC	-67.5	14.6	-	-	*Chin Chem Lett.*

					34, 107788 (2023).
Ru-Co_3O_4-NiO-NF	-67	0.10	1.68	-	*Chem Eng J.* **426**, 131300 (2021).
RuIr@BCN	-66.4	3.84	-	98.5	*Appl Catal, B.* **316**, 121626 (2022).
Ru-CoP/CC	-65	-	-	-	*Angew Chem, Int Ed.* **63**, e202400069 (2024).
Ru-Ni_3N	-63	0.46	-	99.2	*Chem Eng J.* **451**, 138698 (2023).
Ru@Co_2P/CNFs	-59	-	0.61	96.0	*J Alloys Compd* **968**, 171889 (2023).
Ru/CeO_2/C	-57	2.81	-	-	*Appl Surf Sci.* **581**, 152256 (2022).
M-Co@Ru/NC	-56	2.15	4.03	96.0	*Small.* **17**, 2105231 (2021).
Pt/Ru NWs	-55	-	3.45	-	*Adv Powder Mater.* **3**, 100214 (2024).
Pd@RuP	-53	-	-	97.5	*J Energy Chem.* **86**, 510-517 (2023).
Ru/Co_4N/NF	-52	-	-	97.8	*J Mater Chem A* **11**, 22147-22153 (2023).
Ru–MoS_2@PPy	-50.2	6.05	-	-	*Int J Hydrogen Energy* **47**, 37850-37859 (2022).

Ru NP-RuSA@CFN-800	-50	-	11.1	99.0	*Adv Funct Mater* **33**, 2213058 (2023).
V-SRCO	-48.4	-	-	-	*Adv Energy Mater* **13**, 2301779 (2023).
Ru@Ni_3B	-41	-	-	-	*Chem Commun.* **58**, 6741-6744 (2022).
Ru@Ti_3C_2Tx-NS	-38.9	-	-	-	*Int J Hydrogen Energy.* **48**, 9163-9171 (2023).
Ni_5P_4 -Ru/CC	-35	3.83	-	-	*Adv Mater* **32**, 1906972 (2020).
Cu-RuS_2/Ru	-32.6	30.2	-	-	*Mater Today Phys.* **23**, 100625 (2022).
PdRuTe	-29	52	-	-	*Nanoscale.* **14**, 14913-14920 (2022).
RuBNC2000	-27	0.39	10.0	-	*Appl Catal, B.* **353**, 124088 (2024).
Ru/WO_3-W_2N/NC	-21	1.7	-	-	*J Colloid Interface Sci.* **636**, 618-626 (2023).
Ru/TiO_2-VO@C-X	-18	2.9	-	-	*J Mater Chem A* **9**, 10160-10168 (2021).
Ru@CoP/CC-2	-17	-	-	-	*Int J Hydrogen Energy.* **59**, 1205-

1213 (2024).

Table S3. The loading amount of the Ru or M (M=Zn, Fe, Mo, Sm, La) of the tested catalysts obtained by the ICP-OES measurement.

Catalyst	**Ru loading (wt.%)**	**M loading (wt.%)**
ZnO-Ru$_n$/NC	2.36	2.25
Fe_2O_3-Ru$_n$/NC	2.48	2.18
MoO_3-Ru$_n$/NC	2.54	2.53
Sm_2O_3-Ru$_n$/NC	2.47	2.62
La_2O_3-Ru$_n$/NC	2.42	2.56
Zn$_1$-Ru$_n$/NC	2.94	0.31
Fe$_1$-Ru$_n$/NC	2.89	0.30
Mo$_1$-Ru$_n$/NC	2.82	0.32
Sm$_1$-Ru$_n$/NC	2.75	0.41
La$_1$-Ru$_n$/NC	3.07	0.36

Table S4. The mass activity comparison between the La_1-Ru_n/NC catalyst and previously reported Ru-based catalyst at -0.05 V vs. RHE for alkaline HER performed in 1M KOH electrolyte.

Sample	**Ru loading (wt.%)**	**Mass activity (A mg_{Ru}^{-1})**	**Reference**
La_1-Ru_n/NC	3.07	-19.7	This work
Ru-TA/ACC	0.058	ca. -18	*J Mater Chem A.* **7**, 11038-11043 (2019).
Ru NPs/TiN	0.36	ca. -13.5	*Nat Commun.* **15**, 6391 (2024).
UP-$RuNi_{SAs}$/C	1.25 $mg·cm^{-2}$	-12.09	*Nat Commun.* **15**, 2218 (2024).
Ru@Co-NC-800	0.35	-12	*Appl Surf Sci.* **494**, 101-110 (2019).
Ce_1-Ru_n/NC	1	-10.1	*Nat Commun.* **15**, 448 (2024).
Ru_{SA}-O_4/RuNC	6.3	-9.86	*Chem Eng J.* **495**, 153433 (2024).
Ru/P-TiO_2	0.61	ca. -9.7	*Angew Chem, Int Ed.* **134**, e202212196 (2022).
Ru/WC	12.19	-9.33	*J Alloys Compd.* **967**, 171667 (2023).
Ru-Ga_{SA}/N-C	7.98	-9.3	*Nat Commun* **15**, 6741 (2024).
RuBi SAA/Bi@OG	-	-8.5	*Angew Chem, Int Ed.* **62**, e202300879 (2023).
Ru-CrOx@CN	3.8	ca. -8.4	*Nat Catal.* **7**, 441-451 (2024).
Ru-HPC	5.55	-7.8	*Nano Energy.* **58**, 1-10 (2019).
Ru/OMSNNC	1	-7.5	*Adv Mater* **33**, 2006965 (2021).
Ru_{SA}@NiFe PPc	0.7	-6.94	*Energy Environ Sci.* **17**, 1540-1548 (2024).
Ru-ZIF-900	0.18	-6.4	*J Mater Chem A* **8**, 3203-3210 (2020).
Ru/Na^+, K^+-PC	3.1	-6.3	*Nano Res* **16**, 8836-8844 (2023).
RuBNC2000	0.4	-5.8	*Appl Catal, B.* **353**, 124088 (2024).
RuNi/NC	3.9	-5.32	*Nat Commun* **15**, 7179 (2024).
P-Ru/C	11.9	-5.2	*ACS Catal.* **10**, 11751-11757 (2020).

RuCo@Ru$_{SA}$Co$_{SA}$-NMC	1.43	-4.85	*Adv Funct Mater* **33**, 2301804 (2023).
Ordered Ru-Ni	7.08	-4.83	*Chem Eng J.* **487**, 150457 (2024).
Ru$_2$P/WO$_3$/NPC	3.4	-3.95	*Angew Chem, Int Ed.* **133**, 4156-4162 (2021).
Ir-Ru@C	4.3	ca. -3.1	*Appl Catal, B.* **358**, 124422 (2024).
Ru-NPs/SAs@N-TC	0.46	ca. -2.56	*Adv Funct Mater* **30**, 2003007 (2020).
Ru SAs-SnO$_2$/C	3.99	-2.33	*Angew Chem, Int Ed.* **61**, e202209486 (2022).
Ru/d-N-CNT	25 ug·cm^{-2}	-2.3	*Nano Res* **17**, 5261-5269 (2024).
Ru SAs/N-Mo$_2$C	2.39	-1.92	*Appl Catal, B.* **277**, 119236 (2020).
Ru$_1$-Mo$_2$C	34 ug·cm^{-2}	-1.75	*Energy Environ Sci.* **17**, 1397-1406 (2024).
Ru/Mo$_2$C/MoO$_2$	10.78	-1.74	*Adv. Mater. (2024), 2410039. https://doi.org/10.1002/adma.202410039.*
Ru@Cu-TiO$_2$/Cu	52 ug·cm^{-2}	-1.7	*J Am Chem Soc* **145**, 21419-21431 (2023).
HTS-Ru-NCs/TiN	16	-1.68	*Adv Mater* **36**, 2403525 (2024).
Ru/Ru$_x$Fe$_{3-x}$O$_4$	17.3	-1.577	*Nano Lett* **24**, 1015-1023 (2024)
Ru/Zn-NC	2.74	-1.56	*Adv Mater* **36**, 2308798 (2024).
Ni$_{cluster}$-Ru NWs	-	-1.42	*Energy Environ Sci.* **14**, 3194-3202 (2021).
Ru ADC	4.25	-1.25	*Small.* **17**, 2101163 (2021).
S-RuP@NPSC-900	0.8	-0.87	*Adv Sci.* **7**, 2001526 (2020).
RuP/Ru@CNS	48.3	-0.724	*Adv Sci.* **11**, 2309869 (2024).

Ru-CoP/CC	-	-0.7	*Angew Chem, Int Ed.* **63**, e202400069 (2024).
Ru/Ni/WC@NPC	4.13	-0.6	*Adv Energy Mater* **12**, 2200332 (2022).
Ru/B–Ni_2P/Ni_5P_4	6.28	-0.43	*J Mater Chem A* **10**, 16236-16242 (2022).
CNT-V-Fe-Ru	17.84	-0.4	*ACS Catal.* **13**, 49-59 (2023).
Ru@RuP/PC-2	42.5 ug·cm^{-2}	-0.32	*J Mater Chem A* **7**, 5621-5625 (2019).
Ru/Ru,Fe-CoP	10.2	-0.265	*Appl Catal, B.* **352**, 124002 (2024).
Sample Fe_5Ru	223 ug·cm^{-2}	-0.262	*J Colloid Interface Sci.* **659**, 697-706 (2024).
Ru-CrN/NC	8.7	-0.26	*J Mater Chem A* **12**, 8291-8301 (2024).
Ru/MoC@BNC	4	-0.128	*J Mater Chem A* **12**, 19462-19469 (2024).
Ru@Ni-MOF	2.3	-0.125	*Angew Chem, Int Ed.* **60**, 22276-22282 (2021).
c-RP/IP HNT/C	37.92	-0.054	*Adv Energy Mater* **14**, 2401426 (2024).
Ru_3-Ni NPs	32.11	-0.012	*J Colloid Interface Sci.* **678**, 272-280 (2025).

Table S5. The comparison of the cell voltage to afford 1.0 A·cm^{-2} or 0.5 A·cm^{-2} current density and the Ru usage amount between the NF||La_1-Ru_n/NC and previously reported assembly catalysts.

Sample	**M_{noble} loading (ug·cm^{-2})**	**η@0.5 A·cm^{-2}(V)**	**η@1.0 A·cm^{-2}(V)**	**Reference**
La_1-Ru_n/NC	30	1.62	1.68	This work
Ru-LC-$Ni(OH)_2$	1210	1.65	1.69	*Angew Chem, Int Ed.* **136**, e202317220 (2024).
Ru-Ga_{SA}/N-C	80	1.62	1.74	*Nat Commun* **15**, 6741 (2024).
Ru@Cu-TiO_2/Cu	52	1.66	1.77	*J Am Chem Soc* **145**, 21419-21431 (2023).
R-NF-Pt	36.9	1.67	1.77	*Adv Funct Mater* **33**, 2211273 (2023).
MoO_2@Ru NT	158	1.63	1.78	*Adv Energy Mater* **13**, 2301492 (2023).
Ru/Zn-N-C	1000	1.69	1.79	*Adv Mater* **36**, 2308798 (2024).
Ru-Ru_2P/V_2CT_x	360	1.67	1.8	*Appl Catal, B.* **343**, 123517 (2024).
Cl-Pt/LDH	-	1.72	1.87	*Nat Commun* **13**, 6875 (2022).
UP-$RuNi_{SAs}$/C	1154	1.7	1.9	*Nat Commun.* **15**, 2218 (2024).
Pt-AC/Cr-N-C	50	1.78	1.9	*J Am Chem Soc*

				145, 21432-21441 (2023).
Pt-Ru SWNT	34	1.81	-	*Appl Catal, B.* **315**, 121541 (2022).
Ru/NDC-4	80	1.86	-	*Appl Catal, B.* **327**, 122466 (2023).
Turing PtNiNb	50	1.86	1.98	*Nat Commun* **14**, 5389 (2023).
Ru NPs/TiN	-	1.69	2	*Nat Commun* **15**, 6391 (2024).
PtC60	562.5	1.76	2.01	*Nat Commun* **14**, 1711 (2023).
r-Ru-Ni/NiO	107	1.85	2.03	*J Colloid Interface Sci.* **664**, 704-715 (2024).

Supplementary Note 1

The description of the spectroscopic characterizations of the M_xO_y-Ru_n/NC catalysts and the M_1-Ru_n/NC (M=La, Sm, Mo, Fe, Zn) catalysts.

To begin with, as shown in Fig. 3a, we use the Zn LMM Auger measurement to examine the ZnO-Ru_n/NC catalyst because of the severe overlap of Zn 2p XPS peaks between metallic Zn and ZnO.[8] The Zn LMM spectrum of the ZnO-Ru_n/NC catalyst indicates that the Zn species therein with a kinetic energy value of about 988 eV are assigned to the ZnO according to previous report.[9, 10] Furthermore, the X-ray photoelectron spectroscopy technique is employed to characterize the oxidation state of M in other M_xO_y-Ru_n/NC catalysts. As suggested in Fig. 3f, the binding energies of Fe $2p_{3/2}$ (711 eV) and Fe $2p_{1/2}$ (724.6 eV) of the Fe_2O_3-Ru_n/NC catalyst are in good agreement with that of Fe_2O_3.[11] Fig. 3k indicates that the binding energies for the Mo $3d_{5/2}$ (232.4 eV) and the Mo $3d_{3/2}$ (235.5 eV) are in line with that of the MoO_3.[12, 13] Fig. 3p demonstrates that the binding energies for the Sm $3d_{5/2}$ (1083.8 eV) and the Sm $3d_{3/2}$ (1110.8 eV) are attributed to the Sm_2O_3.[14] Fig. 3u displays that the binding energies for the La $3d_{5/2}$ (835.1 eV) and the La $3d_{3/2}$ (852.1 eV) agrees with that of the La_2O_3.[15, 16] These characterizations coupled with the microscopic measurements testifies the united M_xO_y nanocluster and the Ru nanocluster structures of the M_xO_y-Ru_n/NC catalysts. Fig. 3b,c are the Ru K-edge XAFS spectra and the Fourier transforms of the Ru K-edge EXAFS spectra of the Zn_1-Ru_n/NC catalyst and the reference Ru foil and RuO_2, respectively. Fig. 3d,e are the Zn K-edge XAFS spectra and the Fourier transforms of the Zn K-edge EXAFS spectra of the Zn_1-Ru_n/NC catalyst and the reference Zn foil and ZnO, respectively. It is found that the Zn species in the Zn_1-Ru_n/NC catalyst exist in the form of single atom with four N-Zn coordination number as also suggested in Table S1 by the best fitted results while the Ru are in the form of small nanoclusters. Similar XAFS characterizations at the Fe K-edge (Fig. 3i-j), Mo K-edge (Fig. 3n-o), Sm L-edge (Fig.3s-t), and La L-edge (Fig. 3x-y) also confirm the single atom nature of the Fe, Mo, Sm, and La in the Fe_1-Ru_n/NC catalyst, Mo_1-Ru_n/NC catalyst, Sm_1-Ru_n/NC catalyst and La_1-Ru_n/NC catalyst, respectively. These results solidly show the M single atom and Ru nanocluster nature of the M_1-Ru_n/NC catalyst. Because of this, the M_1-Ru_n/NC catalysts and the M_xO_y-Ru_n/NC catalysts can ideally represent for the M_xO_y-Ru_{13} model and the M_1-Ru_{13} model, respectively.

Supplementary References

1. Z. Wang, W. A. Perera, S. Perananthan, J. P. Ferraris and K. J. Balkus, Jr., *ACS Omega*, 2018, **3**, 13913-13918.
2. B. Hu, X. Kang, W. Chen, F. Yang and S. Hu, *CrystEngComm*, 2011, **13**, 1755-1758.
3. Y. Shi, H. Li, L. Wang, W. Shen and H. Chen, *ACS Appl. Mater. Interfaces*, 2012, **4**, 4800-4806.
4. N. Kiomarsipour and R. Shoja Razavi, *Superlattices Microstruct.*, 2012, **52**, 704-710.
5. J. W. Furness, A. D. Kaplan, J. Ning, J. P. Perdew and J. Sun, *J. Phys. Chem. Lett.*, 2020, **11**, 8208-8215.
6. E. Caldeweyher, S. Ehlert, A. Hansen, H. Neugebauer, S. Spicher, C. Bannwarth and S. Grimme, *J. Chem. Phys.*, 2019, **150**.
7. P. E. Blöchl, *Phys. Rev. B*, 1994, **50**, 17953-17979.
8. H. Zhou, X. Yang, L. Li, X. Liu, Y. Huang, X. Pan, A. Wang, J. Li and T. Zhang, *ACS Catal.*, 2016, **6**, 1054-1061.
9. Y. Zhang, N. Lin, Y. Li, X. Wang, H. Wang, J. Kang, R. Wilks, M. Bär and R. Mu, *Sci. Rep.*, 2016, **6**, 23106.
10. P. Kumar, M. C. Mathpal, F. Goutaland, S. A. Hevia, M. M. Duvenhage, W. D. Roos and H. C. Swart, *Mater. Today Chem.*, 2024, **42**, 102371.
11. T. Yamashita and P. Hayes, *Appl. Surf. Sci.*, 2008, **254**, 2441-2449.
12. P. A. Spevack and N. S. McIntyre, *J. Phys. Chem.*, 1993, **97**, 11020-11030.
13. Y. L. Leung, P. C. Wong, M. Y. Zhou, K. A. R. Mitchell and K. J. Smith, *Appl. Surf. Sci.*, 1998, **136**, 178-188.
14. T.-D. Nguyen, D. Mrabet and T.-O. Do, *J. Phys. Chem. C*, 2008, **112**, 15226-15235.
15. B. M. Reddy, P. M. Sreekanth, E. P. Reddy, Y. Yamada, Q. Xu, H. Sakurai and T. Kobayashi, *J. Phys. Chem. B*, 2002, **106**, 5695-5700.
16. V. Patil, K. Agrawal, V. Barhate, S. Patil and A. Mahajan, *Semicond. Sci. Technol.*, 2019, **34**, 034004.